High-frequency broadband active acoustic systems as a tool for highlatitude glacial fjord research

Elizabeth Weidner¹, Grant Deane², Arnaud Le Boyer², Matthew H. Alford², Hari Vishnu³, Mandar Chitre^{3,4}, M. Dale Stokes², Oskar Glowacki⁵, Hayden Johnson², and Fiammetta Straneo⁶

- ¹Department of Marine Sciences, University of Connecticut, Groton, 06340, USA
 - ²Scripps Institution of Oceanography, University of California San Diego, San Diego, 92037, USA
 - ³Acoustic Research Laboratory, National University of Singapore, Singapore, 119227, Singapore
 - ⁴Department of Electrical and Computer Engineering, National University of Singapore, Singapore, 119007, Singapore
 - ⁵Institute of Geophysics, Polish Academy of Sciences, Warsaw, 01-452, Poland
- 10 6School of Engineering and Applied Sciences, Harvard University, Cambridge, 02138, USA

Correspondence to: Elizabeth Weidner (e.weidner@uconn.edu)

Abstract. High-frequency broadband scientific echosounders enable the monitoring of complex dynamics, through rapid collection of high-resolution, near-synoptic observations of the water column and quantitative geophysical measurements. Here, we demonstrate the applicability and utility of broadband active acoustics systems to improve observational capabilities in high-latitude glaciated fjords. These isolated and challenging field locations are a critical environment, linking the terminal end of terrestrial ice fields to the broader ocean, undergoing complex changes due to accelerated high-latitude warming trends. Using broadband (160-240 kHz) acoustic data, collected in tandem with ground truth measurements from a CTD and microstructure probe, in Hornsund fjord in southwest Svalbard we address three topics: 1) variability of the thermohaline structure and mixing across different temporal and spatial scales, 2) identification and characterization of processes in play at dangerous glacier termini, and 3) remote estimation of dissipation rates associated with mixing. Through these analyses, we illustrate the potential of broadband echosounders as a reasonably priced, relatively straightforward addition to experimental field kits, well suited for field deployment in high-latitude fjords where observations are limited by length of season and generally challenging conditions.

1 Introduction

The ice-water interface of marine-terminating (tidewater) glaciers in high-latitude fjords represents a critical transition zone, linking the terrestrial, cryosphere, and ocean systems. As such, tidewater glaciers are central to not only polar but global ocean dynamics: contributing to sea level rise through ablation (Joughin et al., 2012, 2004; Nick et al., 2009), modifying ocean properties through freshwater flux (Fichefet et al., 2003; Straneo et al., 2011), altering thermohaline circulation patterns (Bamber et al., 2012; Beaird et al., 2023; Böning et al., 2016; Slater et al., 2018a; Straneo and Cenedese, 2015), and supporting highly productive and unique marine ecosystems (Hopwood et al., 2020, 2018; Lydersen et al., 2014). Simultaneously, their direct connection to atmospheric and oceanic forcing, combined with accelerated high-latitude warming trends (England et al.,

2021; Holland et al., 2008; Howat et al., 2007; Serreze and Francis, 2006) has resulted in a dramatic increase of glacial retreat rates and ice mass loss over the past two decades (Enderlin and Hamilton, 2014; Geyman et al., 2022; van den Broeke et al., 2016). Despite their importance to polar oceanography, many questions remain in quantifying the impact of changing climate on tidewater glacier systems and predicting the subsequent impact of these changes on the broader polar system (e.g., Straneo and Heimbach, 2013).

A central challenge in characterizing these regions lies in the gap between the observational requirements, both in terms of sampling rate and spatial scale, and current capabilities. High-latitude fiords are isolated, often dangerous environments, where the research season is short, the presence of ice and poor weather limits direct observation, and the field conditions can be physically and psychologically demanding (Leon et al., 2011; Palinkas and Suedfeld, 2008). Moreover, while traditional insitu measurement techniques, such as conductivity-temperature-depth (CTD) or microstructure profilers, can provide highresolution vertical profiles of geophysical measurements (e.g., temperature, salinity), they lack spatial context and practical deployment mechanisms in many regions of high-latitude fjords, e.g., near the ice face. Satellite-based data is commonly used for broad-scale geophysical observations (Konik et al., 2021; Serreze and Stroeve, 2015); however, the spatial resolution of this data can be coarse (>10 m, e.g., Sentinel-2, Landsat-9), depending on the data source. Observations are also often limited by ice and cloud cover and can only provide direct information on the upper meters of the water column (Swift, 1980). These compounded observational challenges often result in qualitative, rather than quantitative, descriptions of critical innerconnected fiord processes, such as the connection between stratification and glacial ablation processes (submarine melting, surface melting, and calving). Enhanced observational capabilities, for both synoptic and in-situ quantitative geophysical measurements, are needed to fill the observational gaps in high-latitude fjords and quantify the ongoing impact of the changing climate. The aim of this manuscript is to outline the potential of broadband scientific echosounders to help address questions regarding geophysical processes in glacier terminus environments and other high-latitude coastal regions.

Active acoustic systems can provide the necessary measurements to improve geophysical observational capabilities in high-latitude glaciated fjords. They offer near-synoptic observations of water column dynamics along km-scale tracks on length scales of shorter than one meter. Acoustic profiles can be collected rapidly, typically at a rate of 0.1-10 Hz, providing coverage of spatial scales from the sub-meters to full-fjord (kms), and temporal scales ranging from seconds to seasons (Godø et al., 2014; Proni and Apel, 1975). Oceanographic processes have a long history of acoustic observation, such as internal waves (Moum et al., 2003; Orr et al., 2000), hydraulic transitions (Cummins et al., 2006; Farmer and Dungan Smith, 1980), stratification (Holbrook et al., 2003; Penrose and Beer, 1981; Ross and Lavery, 2009; Stranne et al., 2017; Weidner et al., 2020), fish and zooplankton communities (Cotter et al., 2021; Foote et al., 2005; Lavery et al., 2010), gas bubbles (Marston et al., 2023; Medwin, 1977; Vagle et al., 2005), suspended sediment (Thorne and Hanes, 2002; Thorne and Hardcastle, 1997; Thorne and Hurther, 2014; Young et al., 1982), and fluid emissions (Bemis et al., 2012; Xu et al., 2017). Active acoustic systems have provided high-resolution bathymetry of polar seas (Björk et al., 2018; Jakobsson et al., 2020), information on fjord circulation patterns (Abib et al., 2024; Sutherland and Straneo, 2012), and information on sea ice extent (Bourke and Garrett, 1987; McLaren et al., 1994; Rothrock and Wensnahan, 2007); however, they remain underused in the study of the

coastal water column, although a number of studies have taken place at lower latitudes (e.g., Bassett et al., 2023; Kilcher and Nash, 2010; Lavery et al., 2013). In this manuscript, we discuss the potential of filling current observational gaps in high-latitude glacial fjord systems using high-frequency (>100 kHz), broadband, scientific split-beam echosounders.

1.1 Overview of scientific echosounders

Scientific echosounders were initially developed as narrowband (single frequency) tools for fisheries applications (e.g., Jech and Michaels, 2006; Simmonds and MacLennan, 2008) and have a long history of producing qualitative plots of acoustic scattering intensity in the water column across both range and depth (echograms); see Fig. 7 in Farmer and Armi (1999), Fig. 1 in Moum et al. (2003), and Fig. 3 in Jech and Michaels (2006). Changes in acoustic scattering intensity, often represented in echograms by a gradated color scale, are driven by changes in acoustic impedance, a combination of medium density and compressibility (e.g., sound speed). Ocean boundaries, such as the seafloor and surface, and water column phenomena, such as biology, ocean structure, and mixing, are common drivers of acoustic impedance changes. Echogram images provide intuitive and compelling qualitative visualization of oceanic processes and boundaries for applications ranging from target identification in recreational fish finders to long-term environmental monitoring by government agencies (e.g., Jech, 2021) to descriptions of hydrological forcing in highly dynamic environments (e.g., Farmer and Armi, 1999). The echosounder used in this work is a split-beam system, where the receive array is split into quadrants to determine the angle of arriving signal through split-aperture processing methods (see Burdic, 1991). Measurements of absolute acoustic scattering strength from split-beam echosounders can be converted into quantitative data streams of important geophysical signals through acoustic inversion methods with the proper field calibration procedure (Demer et al., 2015), in-situ sampling, and theoretical acoustic scattering models. Given the potential for rapid, remote measurements of geophysical properties of the ocean interior, there has been significant effort directed towards developing inversion methods, including analysis of turbulent mixing (Goodman, 1990; Moum et al., 2003; Ross and Lueck, 2005; Seim et al., 1995), seafloor sediment characteristics (Amiri-Simkooei et al., 2011; Fonseca and Mayer, 2007; LeBlanc et al., 1992; McGee, 1990), biomass estimates for fisheries management and community analysis (Martin et al., 1996; Sawada et al., 1993), bubble size distributions (Li et al., 2020), and heat flux from hydrothermal plumes (Xu et al., 2017).

The incorporation of broadband capabilities (signal pulses with an extended and continuous frequency range) has dramatically increased the utility of scientific echosounder systems for the quantitative study of oceanic processes. Compared to narrowband systems, broadband echosounders provide increased along-beam (range) resolution - on the order of decimeters to millimeters - and continuous frequency resolution for spectral characterization (Chu and Stanton, 1998; Ehrenberg and Torkelson, 2000). Increased resolution is leveraged by researchers to discriminate closely spaced targets in the water column, facilitating precise positioning and tracking of targets (e.g., Loranger and Weber, 2020; Weidner et al., 2019; Jerram et al., 2015); while continuous frequency-modulated scattering over the pulse bandwidth reduces the ambiguities in the interpretation of the acoustic returns and specific scattering phenomena can be differentiated and more accurately classified in regions where scattering intensity and spatial context alone are not sufficient (e.g., Lavery et al., 2010; Stanton et al., 2010). Spectral analysis has been leveraged

for acoustic inversion procedures to quantify biomass and determine the community make-up of both plankton (Foote et al., 2005; Lavery et al., 2010) and fish (Cotter et al., 2021; Loranger et al., 2022), as well as differential between multiple scattering mechanisms, for example oil droplets and gas bubbles (Loranger and Weber, 2020). A growing body of literature discusses acoustic inversion methods using commercial broadband echosounders to quantify oceanic phenomena including thermohaline structure (Loranger et al., 2022; Weidner and Weber, 2024), turbulent mixing (Lavery et al., 2013; Muchowski et al., 2022), and gas seeps (Weidner et al., 2019).

1.2 Basics of acoustic data interpretation

100

105

110

115

120

125

130

In the underwater acoustic community, experience and familiarity with acoustic data interpretation methods is assumed, and therefore embedded in the literature. However, the aim of this paper is to expand the use of broadband acoustic tools in coastal polar regions by engaging a broader audience, so here we cover these topics in some detail.

High-resolution, near-synoptic images collected by active acoustic systems are commonly referred to as echograms. Echograms consist of a series of individual time series records of acoustic scattering intensity, typically collected at uniform time intervals. In the case of split-beam echosounders, individual acoustic profiles are measurements of backscattering intensity due to the monostatic geometry of the co-located transmit and receive array (i.e., the transducer, see Medwin and Clay (1997), Section 10.1). When a transducer is mounted on a vessel and data is collected while underway, as in this work, the sequential stacking of closely spaced acoustic profiles effectively provides an "image" in space and time of the water column. In this manuscript, we refer to data collected in this manner as the near-synoptic observations. We use the term near-synoptic because the time interval between individual acoustic records results in an along-track dimension that is always convolved with time, rather than a truly synoptic "snapshot" of the ocean. As a result, observations of non-stationary phenomena (e.g., internal waves, fish schools) can be aliased and this effect should be considered in analysis. Regardless of this complexity, echograms provide highly resolved images of the water column that allow for contextualization and interpretation of oceanic phenomena with resolutions unmatched by other observational means.

There are two types of resolution in an echogram: the along-ray path resolution and along-track resolution. The along-ray path, or range, resolution of an individual acoustic profile is defined by the distance between independent estimates of the backscatter strength. With the application of pulse compression processing techniques, the range resolution of broadband systems is proportional to the inverse of the pulse transducer signal's bandwidth (Chu and Stanton, 1998; Turin, 1960) and typically ranges from millimeter to decimeter scales. The spatial resolution, defined by the distance between individual acoustic profiles in the along-track direction of vessel motion, is a function of the transducer's pulse repetition fire rate (typically 0.1-10 Hz) and duty cycle, the depth of the seafloor, and the speed of the vessel. In nearshore environments, when seafloor depths are relatively shallow (<150 m), typical spacing between profiles ranges from sub-meter to meter-scale.

Echograms offer more than just highly resolved images; they contain quantitative information on ocean water column processes and boundaries. Acoustic energy from the outgoing broadband pulse is scattered and reflected from phenomena in both the water column and at boundaries (e.g., seafloor, sea surface, ice face) that create changes in medium density and sound

speed, referred to in the acoustic literature as impedance contrasts. In the context of the ocean, impedance contrasts are often the result of physical boundaries (see Fig. 2 in Weidner et al., 2020), suspended particulates (plankton, fish, sediment, see Fig. 2 in Cotter et al., 2021 or Fig. 2 in Loranger et al., 2022), changes in thermohaline structure associated pycnoclines (see Fig. 2 in Stranne et al., 2017), and flow or mixing structures (see Fig. 1 in Lavery et al., 2013) within the interior of the water column. Acoustic scattering intensity is often reported in a logarithmic scale (decibels) due to the wide range of potential impedance contrasts associated with ocean boundaries and water column processes. For example, the acoustic scattering intensity recorded from seafloor scattering will be several orders of magnitude higher than scattering from thermohaline structure because the impedance contrast between seawater and rock (or sediment) is significantly greater than the impedance contrast brought about by the transition between water masses. The characteristics of the backscattered signal (e.g., intensity, broadband spectral content) are linked to geophysical properties of oceanic phenomenon (e.g., dissipation rate of turbulent kinetic energy (TKE), bubble size, biological community assemblage), which can be characterized through acoustic data analysis.

1.3 Potential for acoustic measurements in high latitude studies

135

- Broadband scientific echosounders represent a powerful tool for coastal studies; however, until recently the use of broadband analysis methods has been limited in their applicability due to the high cost of custom-made broadband systems, often exceeding \$500,000. The availability of lower cost, commercial broadband systems and the expanded access to a broader user base has resulted in a growing body of literature and processing software for broadband data analysis (Blomberg et al., 2018; Cotter et al., 2019; Demer et al., 2017; Lavery et al., 2017; Weidner et al., 2019). Hence the potential for these systems to improve observational capabilities in isolated and challenging field locations. This paper will address the acoustic analysis of three topics within the study of high-latitude systems:
 - 1) variability of the thermohaline structure and mixing across different temporal and spatial scales,
 - 2) identification and characterization of processes in play at dangerous glacier termini, and
 - 3) remote geophysical parameter estimation.
- 155 Characterizing the distribution of water masses in high-latitude fjords is complicated by the presence of ocean and glacially derived water masses (e.g., submarine melting, subglacial discharge), as well as fjord-scale processes with intense spatial and temporal variability (Hager et al., 2022; Straneo et al., 2011). Elevated levels of vertical mixing in fjords are driven by strong, yet intermittent turbulence associated with the tidal cycle and steep bathymetric features, such as terminal moraines (Farmer and Armi, 1999; Schaffer et al., 2020; Smyth and Moum, 2001). Additionally, the degree of stratification (Geyer and Ralston, 2011), local meteorological conditions (Slater et al., 2018b; Straneo and Cenedese, 2015), and sill-driven reflux (Hager et al., 2022) can influence circulation dynamics and therefore, thermohaline structure.
 - Traditionally, water masses are characterized through the in-situ collection of CTD profiles. Thermohaline structure can be inferred by interpolating between CTD profiles the denser the profile collection, the more accurate the measurements of the spatial distribution of thermohaline structure. Despite their ubiquity and utility, disentangling interconnected processes

controlling thermohaline structure can be challenging using direct observational measurements alone. Individual profiles lack spatial context and dense profile collection can be cost- and time-prohibitive. Acoustic observations can be leveraged to assist in mapping out and characterizing water column structure through imaging of the boundaries (pycnoclines) between water masses. Scattering at water mass boundaries (e.g., pycnoclines) is well documented in the literature and connected to a number of scattering mechanisms, including the sharp gradients in thermohaline structure (e.g., Stranne et al., 2017; Weidner et al., 2020), the intense turbulent mixing due to shear forces (Geyer et al., 2017; Lavery et al., 2013), and the suspended particles, such as biological aggregations (e.g., Benoit-Bird et al., 2009) or sediment (e.g., Simmons et al., 2020), that are often associated with thermohaline structure. The inclusion of broadband acoustic data together with direct sampling can elucidate the fjord-scale dynamics that control the distribution of thermohaline structure.

175

180

185

190

195

Beyond the near-synoptic observations, echosounders can collect measurements in regions inaccessible to direct sampling equipment. In high-latitude glacial fjords, this remote advantage can be leveraged to collect measurements in dangerous regions, such as a submerged ice-ocean interface of the glacial terminus. Direct observations at the ice edge in literature are few owing to limited access by the presence of ice mélange and icebergs. Furthermore, calving events, both subaerial and submarine, make work at the ice face dangerous for vessels, equipment, and personnel, and preclude most ship-based sampling. Oceanographic data, such as CTD casts, are generally collected downstream in the fjord and ice-ocean dynamics are then inferred (Beaird et al., 2023; Stevens et al., 2016; Straneo et al., 2011). The few in-situ observations have been collected by helicopters (Bendtsen et al., 2015), remotely operated vehicles (Mankoff et al., 2016), and sensors attached to marine mammals (Everett et al., 2018). The paucity of direct measurements limits the inclusion of terminus ice-ocean dynamics in large-scale climate models (Bamber et al., 2018), predictions of fjord circulation (Straneo et al., 2011), and contribution to sea level rise predictions (Siegert et al., 2020). The need for enhanced observational capabilities and additional measurements at the ice-ocean interface has been well documented, e.g. by Siegert et al. (2020).

A number of recent studies have employed acoustic systems to overcome the challenges associated with near-terminus observations. Sutherland et al., (2019) estimated submarine melt rates by combining high-resolution images of the submerged terminus from a multibeam echosounder with data on glacier motion. An acoustic Doppler current profiler (ADCP) deployed from an autonomous surface vehicle by Jackson et al. (2020), provided the first characterization of meltwater intrusions in the near-terminus region. Broadband echosounders can add to this acoustic toolset by providing remote, quantitative observations of the ice-ocean interface and those processes occurring nearby, such as subglacial discharge. Broadband echosounders uniquely can make measurements of absolute scattering intensity, not possible with other acoustic systems, and these measurements, combined with split-aperture processing and broadband spectral analysis, can shed light on the morphology of the terminus, identify the presence and constrain the geometry of subglacial discharge plumes, and identify inner-connection bio-physical processes occurring near the terminus.

Finally, quantitative analysis of broadband spectral data can be used to identify scattering mechanisms and even provide remote measurements of geophysical signals (e.g., dissipation rates of TKE, gas bubble size). These methods compare the calibrated, absolute scattering measurements of a specific phenomenon made by field echosounders to predicted scattering levels from

theoretical acoustic scattering models. The models are generally informed by in-situ measurements of the physical (e.g., thermohaline structure, bubbles, suspended sediments) or biological scattering mechanisms, collected in tandem with the acoustic field measurements. The direct comparison of scattering levels allows for inversion for geophysical parameters from rapid, high-resolution, near synoptic, echosounder observations and offers a promising alternative to traditional direct sampling approaches in challenging locations.

The aim of this paper is to demonstrate the applicability and utility of active acoustics systems to high-latitude systems using a high-frequency (160-240 kHz), broadband acoustic dataset collected in Hornsund fjord, Svalbard. Section 2 of this paper provides an overview of the field site in Svalbard. The equipment, vessel, and data collection methods are described in Section 3. Section 4 covers the analysis of high-resolution water column observations in tandem with direct sampling to characterize dynamics across the full-fjord scale, as well as the potential for remote measurements in the dangerous region of the submerged glacial terminus. Section 4 also includes a discussion of broadband spectral analysis and acoustic inversion efforts to remotely measure turbulent mixing associated with fjord bathymetry and tidal forcing. A discussion of the acoustic data collection methods and analysis, including safety considerations for glacial systems and limitations of broadband systems is covered in Section 5. Section 6 concludes the paper with the potential for future applications of broadband systems to high-latitude fjords.

2 Study site

200

205

210

225

230

Hornsund fjord is a highly glaciated, ~35 km long fjord located in southwest Spitsbergen, Svalbard (Fig. 1). Glaciers cover approximately 67% (802 km²) of the total area of Hornsund fjord, with tidewater glaciers constituting 97% of its glacierized area (Błaszczyk et al., 2013). The western coast of Svalbard, including Hornsund Fjord, is influenced mainly by the North Atlantic Ocean current (Walczowski and Piechura 2006). The mean annual air temperature trend of the region over the last four decades is more than +1.14 °C decade⁻¹, a rate six times higher than the global average (Wawrzyniak and Osuch, 2020). Tidewater glaciers in Hornsund Fjord are retreating at an average rate of ~70-100 m yr⁻¹ (Błaszczyk et al., 2023, 2013), which is among the highest rates in Svalbard.

Data collection in Hornsund took place in the glaciated bay of Hansbukta and at the calving front of the retreating, grounded tidewater glacier Hansbreen. The bathymetry of Hansbukta is dominated by rapid shallowing from a main channel of Hornsund fjord (~200 m deep) to a well-defined transverse ridge (3-15 m deep), which is interpreted as the terminal moraine of Hansbreen (Ćwiąkała et al., 2018). A series of smaller transverse ridges, plough marks, depression areas, and pockmarks characterize the bathymetry of inner Hansbukta approaching the terminus of Hansbreen. Hansbreen is a polythermal glacier with a mixed basal thermal regime and covers an area of ~54 km² (Błaszczyk et al., 2013). The calving front of Hansbreen is 1.7 km long (Błaszczyk et al., 2019), grounding at ~70 m depth, and has retreated on average 38 m yr¹ between 1992-2015 (with a maximum rate of 311 m yr¹), which is more than twice its historical rate (Błaszczyk et al., 2021; Grabiec et al., 2018). Svalbard's enhanced warming trends combined with Hansbreen's long history of study (e.g., Kosiba, 1960) and close proximity to the Polish Polar Station Hornsund makes this an excellent field site for acoustic data collection and methods.

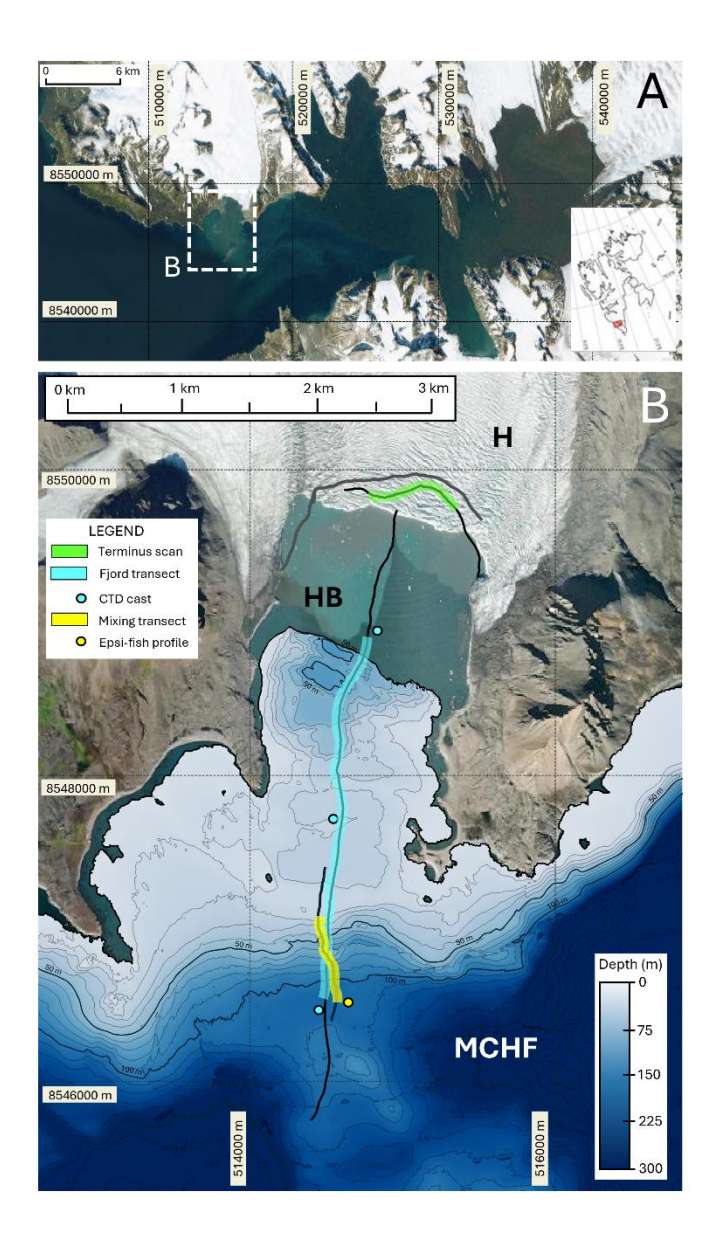


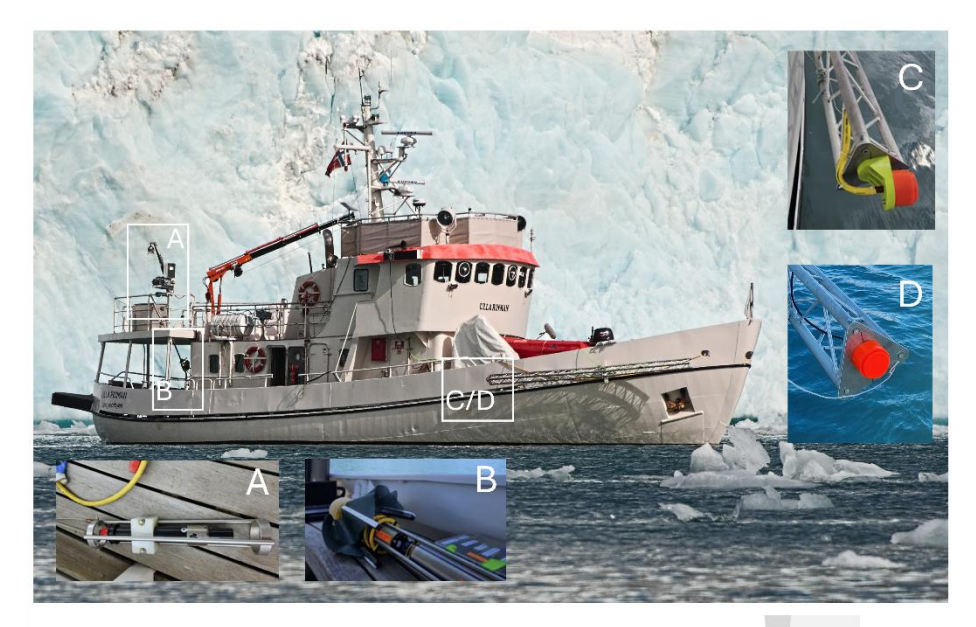
Figure 1: The general location of 2023 field program in Hornsund Fjord, Spitsbergen, Svalbard (A). The region of study in Hornsund fjord is identified by the inset box B and is illustrated in the lower image. The background image is from Landsat–8 imagery collected in June 2023, courtesy of the U.S. Geological Survey, Department of the Interior. Multibeam bathymetry of Hornsund fjord (MCHF) and Hansbugta (HB) is provided by Blaszczyk et al. (2020) and the Norwegian Hydrographic Service. Bathymetric coverage of Hansbukta does not fully cover the region of study due to the retreat of Hansbreen (H) since the most recent seafloor survey. The position of Hansbreen's terminus during operations in July 2023 was estimated using MV Ulla Rinman's radar and is denoted by the grey line. The black lines running north-south across Hansbugta and parallel to Hansbreen are the tracks of MV Ulla Rinman during the broadband acoustic data collection. Highlighted regions identify the extent of echograms from Fig. 3 (blue), Fig. 4 (green), and Fig. 5 (yellow). Circular markers are the positions of the CTD casts (Fig. 3) and Epsi-fish profile (Fig. 5).

3 Data collection methods

245

Data were collected between July 6th and 12th, 2023 onboard the Marine Vessel (MV) Ulla Rinman and included broadband acoustic backscattering data throughout the water column, conductivity-temperature-depth (CTD) profiles, microstructure casts, and time-lapse imagery (Fig. 2). Acoustic data were collected with a Simrad EK80 wideband transceiver transmitting with a Simrad ES200-7CD split-beam transducer with a 7° circular beam and frequency range of 160-240 kHz. The transducer was deployed from a 6 meter-long side-mount pole with two geometries during the field campaign: downward- and sidelooking. The transducer was mounted directly to the vertical pole for the downward looking geometry. For the side-looking geometry, a 3-dimensional (3-D) printed plate adaptor provided a 10° declination angle relative to the horizontal. The system 250 was operated continuously during survey operations and all acoustic system parameters (i.e., transmit power, signal mode, pulse length, frequency range) were kept constant during acquisition. The acoustic system was calibrated using a 25.0 mm tungsten-carbine sphere during field operations on 6 July 2023 and in the Chase Engineering Tank at the University of New Hampshire with 25.0 mm and 38.1 mm tungsten-carbine spheres on 13 March 2024, following the procedure described in Demer et al. (2015).

- 255 Position and attitude data were collected and applied to the field data in post processing from a SBG system Ellipse-D Inertial Navigation System (INS). The INS was mobilized on the bridge, and the antennas were mobilized on the bridge deck railing of MV Ulla Rinman, with a clear sky view and more than 2 meters of separation. The INS provided horizontal and vertical positioning accuracies of 1.2 m and 1.5 m respectively. Pitch and roll accuracies were 0.1° and heading accuracy was 0.2° for 1 m baseline.
- 260 Ground truth data was collected by two in-situ sensors, a Valeport miniCTD sensor and an Epsilometer microstructure probe, "Epsi-fish" (Le Boyer et al 2021). The Valeport miniCTD unit provided vertical profiles of water column temperature and salinity and was deployed via MV Ulla Rinman's winch. The accuracies of the pressure, conductivity, and temperature measurements from the Valeport miniCTD unit were ±0.05% of full range (300 m), ±0.01 mS/m, and ±0.01°C, respectively. The Epsi-fish, deployed from a commercial fishing reel, provided a total of seven profiles of thermal (χ_T) and turbulent kinetic 265 energy (e) dissipation rates. The Epsi-fish, which provided measurements of thermal and kinetic energy dissipation rates, was developed at Scripps Institution of Oceanography by the Multiscale Ocean Dynamics group. A full description of the Epsifish sensors, accuracies, and deployment considerations can be found in LeBoyer et al., (2021). Additionally, two GoPro Herol1 time lapse cameras were deployed to capture images of ice coverage (ice mélange and icebergs) and other surface expressions in the fjord during survey operations. A complete description of the field deployment, data collection procedure 270 and data processing details can be found in Appendices A and B.



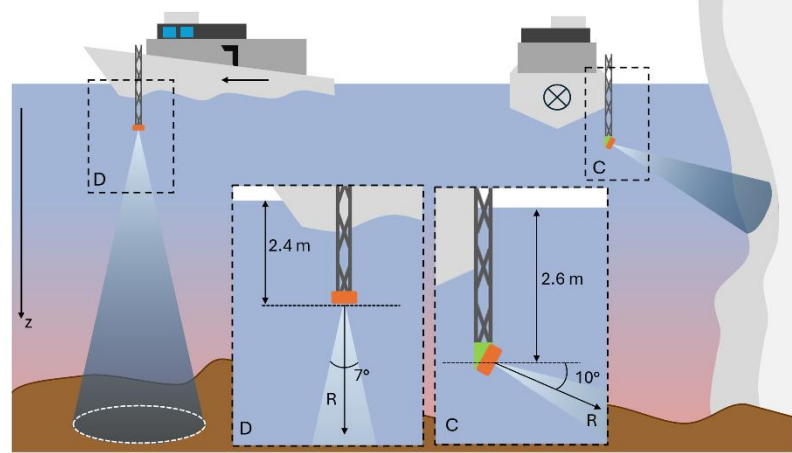


Figure 2: The acoustic survey platform, MV Ulla Rinman. The ground truth systems, CTD and microstructure profiler, were deployed from the starboard aft of the ship. Inset box A illustrates the deployment set up for the CTD sensor using ship's winch.

Inset box B illustrates the microstructure probe deployment site from a commercial fishing reel. The broadband acoustic transducer was deployed forward, on the starboard side by a side-mounted pole in two geometries, inset box C/D in the top image. The side-looking geometry (box C) used a 3-D printed mount plate adaptor to achieve a 10° declination angle from horizontal and was used to collect acoustic scans of the submerged ice face of Hansbreen. The downward-looking geometry (box D) was used to collect fjord-scale transects.

4 Interpretation and analysis of broadband echosounder data

280

Broadband echosounder data collected in Hornsund fjord is here used to demonstrate methods for backscatter data interpretation and analysis in the following sections: the contextualization and characterization of fjord-scale thermohaline structure using acoustic observations and direct sampling (Section 4.1), leveraging the remote nature of acoustic measurements

to observe the largely inaccessible submerged terminus (Section 4.2), and the quantitative analysis of tidally and bathymetrically forced mixing through broadband acoustic inversion methods (Section 4.3).

4.1 Characterizing thermohaline structure in Hansbukta

285

290

295

300

Acoustic transects of Hansbukta were collected alongside in-situ sampling with the miniCTD sensor. The acoustic transects ran along a north-south heading from the deep channel at the mouth of Hornsund Fjord into Hansbukta to the submerged terminus of Hansbreen (see Fig. 1). The echogram in Fig. 3 illustrates a section of one such transect, approximately 1.7 km long and collected over a period of 35 minutes during the peak ebb tide. The complex, glacially derived bathymetry of Hansbukta is captured and is the strongest scatterer in the echogram (>-20 dB re m⁻¹). Running from south to north, the bathymetry transitions from the deep (>200 m) main channel of Hornsund fjord to the glacial trough of Hansbreen, where the grounding line is approximately 65 m deep. Between the main channel and Hansbreen the seafloor shallows rapidly over a series of sills, transitioning rapidly from >200 m to 12 m in depth over less than 250 m along track. In the water column numerous scattering phenomenon are represented. Biological scattering from individual fish and aggregations are observable, primarily in the main channel (1400-1700 m along track) and glacial trough (0-200 m along track), as discrete and small features or larger semi-circular regions of elevated scattering between -25 and -35 dB re m⁻¹. Scattering associated with the evolving thermohaline structure across Hansbukta is also observable as weakly scattering (<-50 dB re m⁻¹) semi-discrete layers in the upper 20 m of the water column. Several layer-like features evolve over the length of the transect and are discussed below using the CTD data for context. Three miniCTD profiles were collected at key locations along the transect: in the main channel, at the shallowest point of the primary sill, and in the inner fjord. The CTD profiles provide direct measurements of the thermohaline structure at discrete locations across Hansbukta, while the broadband echogram provides spatial context on water mass evolution and the hydrodynamic processes influencing thermohaline structure.

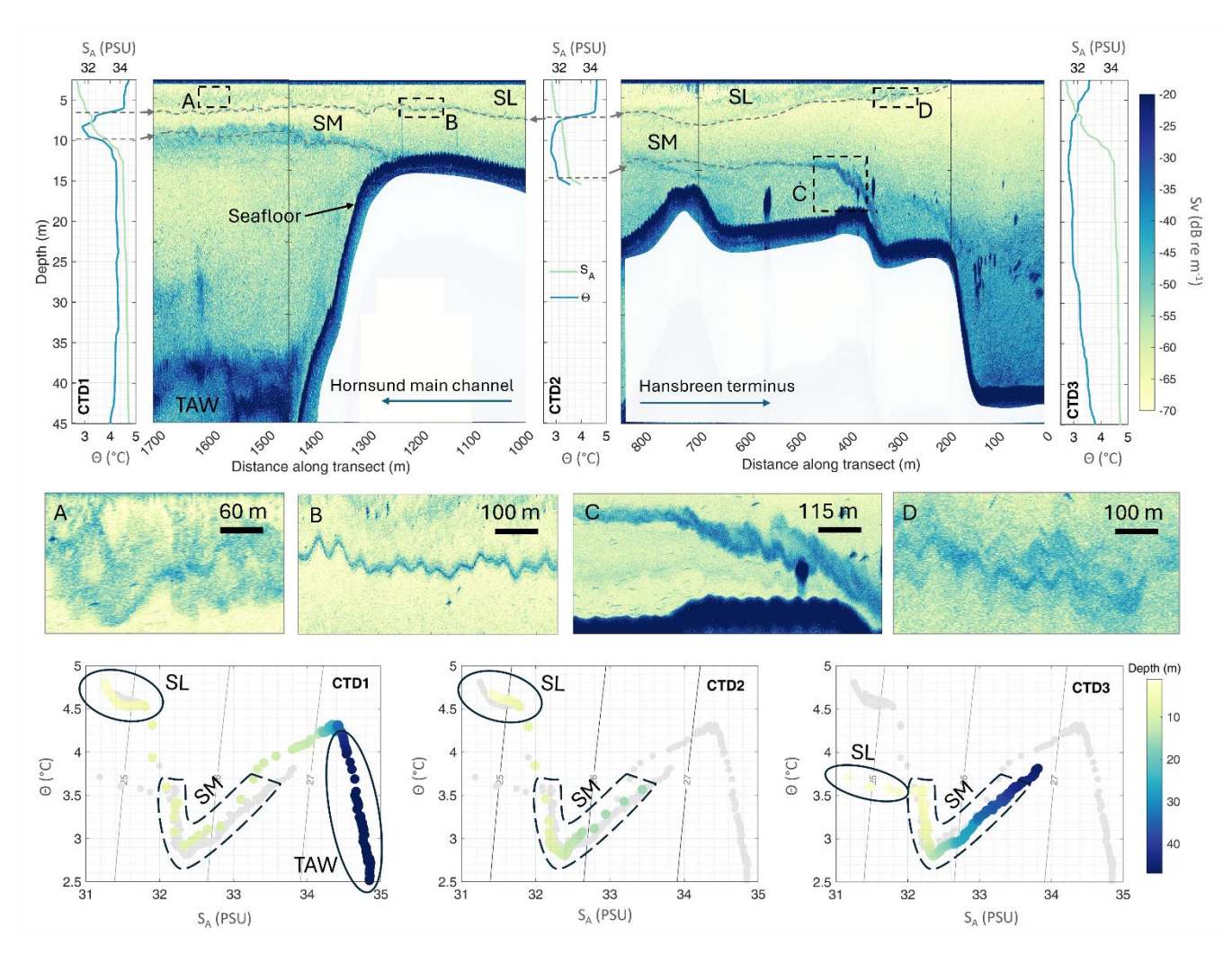


Figure 3: The top panel is an example broadband acoustic transect collected in Hansbukta over the shallow sills separating Hansbreen (far right) from the primary channel of Hornsund fjord (far left). See Figure 1 (blue highlighted transect lines and blue markers) for transect and CTD cast locations within the larger study site. The echogram is colored in a logarithmic scale by volumetric scattering strength (Sv) Three CTD casts were collected, at the beginning (CTD 1) and end of the transect (CTD 3), as well as at the shallow point of the terminal moraine of Hansbreen (CTD 2). The CTD profiles of conservative temperature (Θ) and absolute salinity (S_A) are plotted against depth in their approximate cast position with reference to the acoustic transect. During CTD cast collection the acoustic data collection was paused, resulting in the break in the echogram over the sill. The maximum depth of the echogram was limited to 45 m to best illustrate the area of interest in thermohaline structure. Regions of particular interest are highlighted in boxes A-D and zoomed in views are illustrated below the echogram. The bottom set of panels show the temperature-salinity (T-S) diagrams, illustrating the connectivity of waters across Hansbukta and the influence of specific water masses. T-S diagrams plot absolute salinity against conservative temperature for all three CTD casts, colored by depth. On each plot the T-S data from the other two casts is plotted in light gray for comparative purposes. Specific water masses are noted, including Transformed Atlantic Water (TAW), region influenced by sill mixing (SM), and the surface layer (SL).

Generally, thermohaline structure in Hansbukta can be influenced by two external water masses: Atlantic water (AW) transported on the West Spitsbergen Current, characterized as both warm and saline (3.5 to 6.0°C, >35 PSU) (Strzelewicz et al., 2022; Walczowski, 2013), and the relatively cold and saline waters (-1.5 to 1.5°C, 34.3 to 34.8 PSU) originating from

western Svalbard carried on the Sorkapp Current (SC) (Cottier et al., 2005; Promińska et al., 2018). Additionally, submarine glacial discharge and submarine meltwater from ablation, melting and runoff associated with Hansbreen are introduced into the glacial trough of Hansbukta. Discharge rates from Hansbreen are variable depending on the season, primarily peaking between June and September (Błaszczyk et al., 2019).

325

330

335

340

345

The three CTD casts can fingerprint the external and glacially influenced water masses and provide a coarse view of the distribution of thermohaline structure across Hansbukta. At the southernmost extent of the transect in the main channel of Hornsund Fjord (>20 m) the CTD profile shows that the deep water column can be described as transformed Atlantic water (TAW – Fig. 3), the product of entrainments and mixing between AW and SC waters (Nilsen et al., 2008); however, the cold and saline TAW waters are isolated by the shallow sill of Hansbukta and are absent in the sill and glacial trough CTD profiles. At the surface, all the CTD profiles show a well-mixed surface layer (SL – Fig. 3), characterized by relatively warm and fresh water, likely influenced by submarine glacial discharge and submarine meltwater from Hansbreen. The vertical extent of SL water deepens and warms between the glacial trough and the sills, from 2.0 to 7.5 meters in depth and from 3.6°C to 4.7°C, and then retains the same depth and T-S characteristics between the sill and main channel. Below the surface layer, the thermohaline structure of the water column from the main channel of Hornsund fjord, over the sills, to the glacial trough shows nearly identical T-S characteristics, influenced by sill mixing (SM – Fig. 3). SM water is defined by increasing salinity and a temperature inversion with increasing depth. SM water has a minimum temperature of 2.7°C and shallows in depth from 12.2 to 6.5 meters between the glacial trough and the sill CTD casts. It extends over the water column of the sills and glacial trough CTD casts from the base of the submarine glacial discharge -influenced surface layer to the seafloor, while in the main channel it is bounded by a depth approximately equal to that of the shallowest sill depth (~12 m). Overall, the CTD data suggests the influence of Hansbreen extends across Hansbukta well into the main channel of Hornsund fiord evidenced by the persistent, low-salinity SL water across all casts. Furthermore, there is evidence of strong connectivity between the deeper SM water mass in the glacial trough of Hansbukta and in the main channel of Hornsund fiord; SM water is characterized by the low temperature intrusion layer seen in all three T-S plots. SM water is constrained by the sill depth in the main channel, suggesting a bathymetric control on not only the thermohaline structure but the transport of heat and salt between the main channel of Hornsund and the inner bay of Hansbukta and the ice-ocean interface of Hansbreen. However, without additional casts or other information, disentangling the interconnected processes that are controlling the spatial distribution of SL, SM, and TAW water in Hansbukta and the broader transport of heat and salt across Hornsund fjord (e.g., tides, bathymetry, glacial discharge rates) remains out of reach.

The broadband acoustic data collected between the CTD casts offers the potential to more fully characterize the distribution of thermohaline structure across Hansbukta and start to explain the dynamics behind evolution observed in the in-situ profiles. The water mass boundaries identified by the CTD casts are clearly visible in the echogram as regions of elevated scattering, as illustrated by the gray dashed lines in Fig. 3. The mechanism in the water column responsible for the elevated scattering signal is not immediately clear from visual inspection of the echogram and could be tied to a number of processes (e.g., gradients in T-S, mixing, biological or sediment particulates); however, these regions show general agreement in their position

(depth) with the in-situ data on water mass boundaries. Unlike the in-situ data, the echogram allows for precise positioning of the visible boundaries across the entire transect of Hansbukta and the nature of the scattered signal (e.g., shape, intensity) provides context on the active mixing processes occurring in the water column.

360

365

370

375

380

385

Starting with the surface layer, SL waters can be identified by the scattering associated with the sharp gradient in temperature and salinity that occurs at the boundary between the base of the surface and the intermediate water mass below. While this boundary is not visible in the glacial trough (<200 m along track) because the depth of the surface layer is shallower than the draft plus blanking distance of the transducer, beyond this point the boundary can be tracked as it progressively deepens from the glacial trough over the sills and to the main channel. The nature of the scattering associated with this boundary evolves along track, elucidating the processes that modify the water mass, as measured in the CTD casts. At the onset of the sills, the boundary is characterized by a series of Kelvin-Helmholtz (KH) instabilities (Fig. 3, inset box A), recognized by their alternating braid-core structure (e.g., Thorpe, 1987; van Haren and Gostiaux, 2010). KH instabilities are regions of intense shear and turbulent mixing and have been imaged acoustically in other highly energetic coastal regions (Gever et al., 2017; Lavery et al., 2013). Here, the shear is likely generated by the south flowing current at the surface driven by the ebb tide, potentially combined with the shallowing bathymetry of the sills, evidenced by the presence and directionality of the KH shear instability structure. The mixing between the surface layer and the intermediate water mass below explains the deepening and change in surface layer properties observed in the CTD casts. Beyond the sills, starting at 1000 m along track (Fig. 3), the boundary of the surface layer becomes a discrete, thin scattering layer. The lack of KH instabilities, suggests scattering from a sharp gradient associated with the pycnocline (e.g., Stranne et al., 2017; Weidner et al., 2020), with little mixing or modification in the boundary properties; these observations suggest the surface layer should have similar T-S properties between the sill and main channel, as was observed in the CTD profiles.

Deeper in the water column there is intense scattering from KH shear instabilities closely associated with the rapid changes in bathymetry at either end of the sills (Fig. 3). In the inner fjord at the onset of each sill, trains of KH instabilities are visible, closely tracking the seafloor depth. The strongest scattering is associated with the second sill, starting at approximately 300 m along track. Given the close contact with the seafloor, the elevated scattering levels associated with the KH instabilities could be driven by resuspended sediment from strong currents, entrained organisms, or from turbulent microstructure; in either case, the observations from the echogram points to intense mixing in the inner fjord near the seafloor and transport of water across the sills, likely driven primarily by the changing tide. On the far side of the outermost sill, entering the main channel of Hornsund fjord, there is a region of elevated scattering centered at approximately 10 m depth that starts at the sill edge and continues for an along track distance of more than 400 m to the end of the echogram record (Fig. 3). The depth of elevated scattering matches the base of the intermediate water mass identified in the CTD casts by the strong temperature inversion, while the nature of the scattered signal points to an active mixing process although the braided structure of KH instabilities is not as clear as those in the inner sill area. Again, observations from the echogram point to water mass transport over the sill and explain the connection in T-S properties between the intermediate waters of the main channel of Hornsund fjord and the inner bay of Hansbukta in the glacial trough.

390 Overall, the combination of the near-synoptic acoustic observations and the in-situ CTD measurements point to a combination of tidally induced flow and the shallow sills controlling the intermediate thermohaline structure across Hansbukta, while a surface layer influenced by submarine glacial discharge is persistent throughout Hansbukta. Tidal pumping is identified as the driving process for water mass transport and transformation from 1) the presence and directionality of the KH instabilities that develop at the interface between water masses and the sills as imaged in the echogram, and 2) the resulting connectivity of thermohaline structure measured directly by the CTD casts. This type of stratified flow over topography is well defined in the 395 literature (e.g., Farmer and Armi, 1999; Geyer et al., 2017) and has been observed in estuaries, as well as in terrestrial systems such as mountain ranges (Lilly, 1978). This conclusion is supported by previous research in Hornsund fjord, which suggests that tidal forcing is the main hydrodynamic driver of heat, salt and fresh water budgets (Jakacki et al., 2017; Kowalik et al., 2015). The analysis of Fig. 3 transect illustrates the utility of broadband echosounder data as a contextual tool for the study of 400 high-latitude systems and the importance of direct sampling sensors, such as CTDs to inform the analysis and vice versa. The CTD profiles lack the high-resolution spatial context to directly determine the dynamics driving the thermohaline variability, while the acoustic observations are inherently ambiguous, requiring ground truth information for a complete analysis. Here, a combination of the near-synoptic acoustic observations with the in-situ measurements of the thermohaline structure can provide important physical context for interpretation of the driving oceanographic processes.

4.2 Remote observations of the ice-ocean interface

405

410

415

Measurements of the submerged terminus of Hansbreen were collected using a side-looking geometry (Fig. 2). A series of survey lines were run for approximately 1.2 km parallel to the ice face from east to west, limited by the shallowing seafloor edges of Hansbukta. The transducer geometry provided a diagonal slice of water column observations starting at 2.6 m depth (transducer draft) to between 17-25 meters deep at the submerged terminus (see Appendix B for additional information). The resulting echogram provides imagery of the submerged terminus, as well as near-terminus water column phenomena occurring between the transducer and the ice face, including scattering from subglacial discharge (Fig. 4). Concurrently with broadband data collection, water surface imagery was collected with a time-lapse camera. During survey operations near Hansbreen the surface expression of a subglacial discharge plume was observed as a persistent ice-free region extending outwards from the ice face <200 m. No surface flow velocity measurements were made but a distinct boundary was observed at the edge of the plume, marked by the ring of ice mélange and a change in surface texture. Observations are consistent with the surfacing of buoyant subglacial discharge reported in the literature (Chauché et al., 2014; Mankoff et al., 2016; Mortensen et al., 2013; Motyka et al., 2003; Xu et al., 2013)

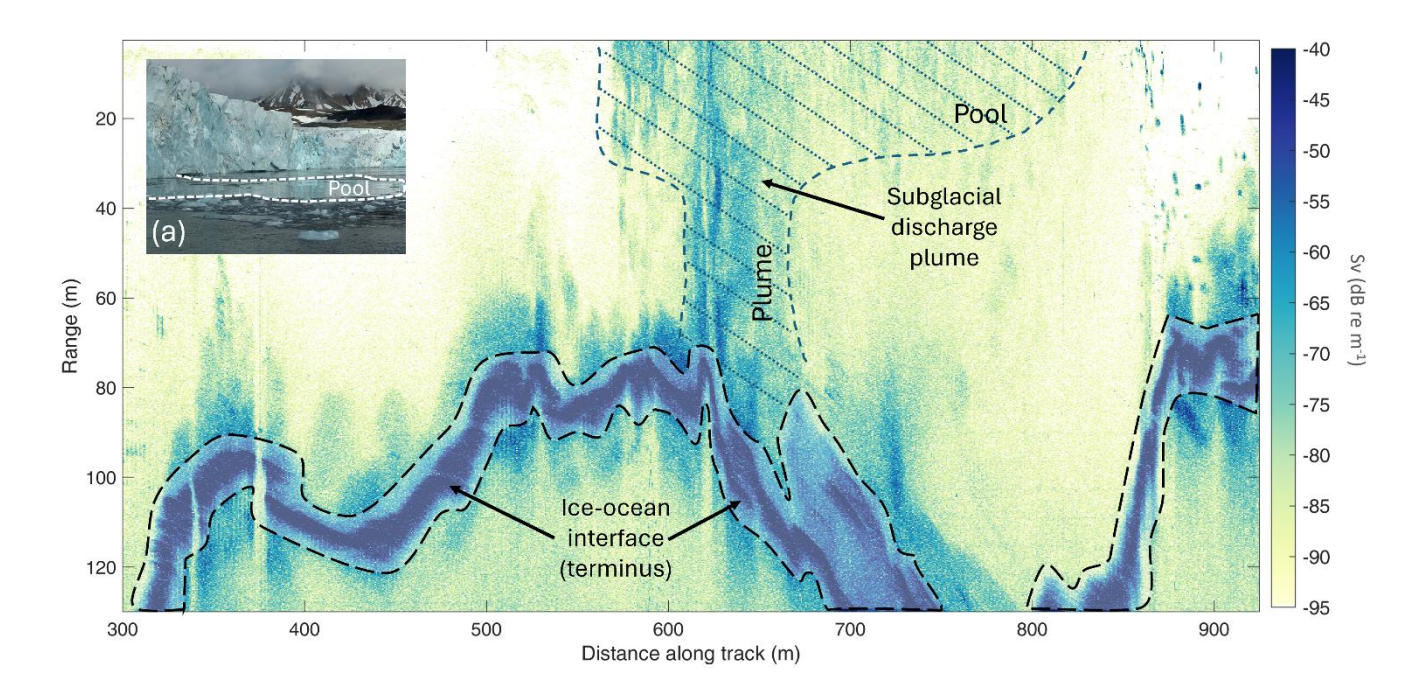


Figure 4: Broadband acoustic observations of the submerged terminus of Hansbreen and the surface expression from the time-lapse imagery (inset box A). See Fig. 1 (green highlighted transect lines) for transect location within the larger study site. The ice-ocean interface of Hansbreen is the bounded by the thick black dashed line. The submerged expression of the subglacial discharge plume and its evolution to the surface pool is marked by the dark blue dashed line; the plume and pool extent were determined from manual interpretation of the elevated scattering intensity in the water column. Potential subglacial discharge, which does not reach the surface, may also be located between 350-400 m along track.

Broadband echosounders can precisely position the submerged terminus, as well as provide measurements of the ice face along-track geometry (Fig. 4). In the echogram the terminus is easily identifiable across the entire transect by an elongated, strong backscattering return (>-40 dB re m⁻¹) starting between 75 to 120 meters in range. The elongated return from the submerged ice face is initially characterized by the side lobe return, a weakly scattering signal of a variable length (i.e., between approximately 475-550 m and 675-700 m along track). The primary return from the submerged terminus shows a generally monotonic increase to a peak intensity value, before a gradual reduction in intensity. The length of the primary return is variable, likely due to variability in the angle of ice face tilt with respect to the transducer. This type of elongated return resulting from oblique incidence geometry and the propagation of the acoustic pulse along an extended surface target has been observed in other broadband echosounder work (e.g., Weber and Ward, 2015), as well as in multibeam echosounders at large incidence angle (e.g., Lurton, 2002 Fig. 8.30). Tracking the terminus position can provide a direct measurement of submerged terminus geometry, such as trends in the over- or -under-cutting of the submerged ice face (e.g., Weidner, 2025; Abib et al., 2023; Sutherland et al., 2019; Rignot et al., 2010; Robertson et al., 2012; Sugiyama et al., 2019).

430

In addition to observations of the submerged terminus, elevated backscattering from subglacial discharge can be seen in the echogram between 575 and 825 meters along the transect. The geometry of the subglacial discharge evolves as it rises in the water column towards the surface. Initially, the region of elevated scattering extends outwards from the submerged terminus in a narrow core approximately 50 meters across (620 to 675 meters along track), referred to here as the "plume" region following Mankoff et al. (2016). This plume extends outward from the ice face 40 to 50 meters with little change in its along-track width (parallel to the ice face). At a range from the transducer of approximately 25 meters, 7 meters depth, the plume rapidly expands to a region more than 300 meters across, referred to here as the "pool". The position and extent (distance along-calving front) of the surface expression of the subglacial discharge pool, observed from the deck of MV Ulla Rinman and in the time-lapse imagery, show agreement with the acoustic measurements. To our knowledge, these are the most detailed measurements, acoustic or otherwise, of the geometry of a subglacial discharge event. Measurements such as these can provide direct information about the variability in plume width, which strongly affects the plume neutral buoyancy depth, upwelling flux, and plume-driven renewal time (Slater et al., 2022). Future analysis could take advantage of split-aperture processing techniques employed for gas seep plumes (e.g., Blomberg et al., 2018; Jerram et al., 2015) to determine the position and geometry of the plume and submerged ice face more precisely.

Beyond spatial measurements of the discharge, broadband acoustic observations can elucidate the dynamics of subglacial discharge plumes, by acquiring data that reveals the scale and geometry of the discharge location at the grounding line. It is well established that fresh water from surface melting, precipitation events, and other terrestrial inputs is channelled upstream of the terminus and is injected into the fjord environment at the calving front; however, the nature of the discharge location, whether at single or multiple distinct locations (point source) or across the length of the terminus (line source) remains unanswered (Jenkins, 2011; Mugford and Dowdeswell, 2011; Sciascia et al., 2013; Xu et al., 2013, 2012). The geometry of the discharge location defines the plume evolution and subsequently the entrainment rate of ambient fjord water, the total area of enhanced submarine melt rates due to plume-ice interaction, and the spread of glacially modified waters at the depth of hydrostatic equilibrium (Motyka et al., 2003; Wagner et al., 2019). Moreover, geometry is an important component of the parameterization of plume dynamics for fjord-scale modeling (Cowton et al., 2015; Slater et al., 2020). Acoustic systems can provide direct observations of the subglacial discharge location and the backscattering signal from the plume higher in the water column can provide important observations related to plume dynamics (e.g., entrainment rates, scale of overturning).

Acoustic observations from Hansbukta demonstrate echosounders can verify the presence of subglacial discharge in the water column. In Hansbukta the submerged expression of discharge coincided with a surface expression. Prior to this work, the detection of the presence of subglacial discharge plumes depended on visible surface expression of sediment laden waters (e.g., Chauché et al., 2014); however, at termini with deeper grounding lines surface expression is not always expected (e.g., Stevens et al., 2016). Recent modeling work from Slater et al. (2022) indicates that only 28% of subglacial discharge plumes in Greenland reach a neutral buoyancy in the photic zone due to a combination of near-terminus stratification and weak discharge. The Slater et al. (2022) results suggest that more than two-thirds of cases plume dynamics are under accounted for in modeling efforts of ice-ocean interactions, including increased submarine melt and calving rates; this does not even account

for the fact that a plume reaching the photic zone does not guarantee that it will have a visible surface expression. Again, broadband echosounders offer the means to close these observational gaps by providing remote verification of plume presence, as well as help better understand the dependency of plume dynamics on the slope of the submerged terminus (Jenkins, 2011), identify the plume neutral buoyancy depth, and impact on downstream thermohaline structure, and plume and terminus geometry.

Any data collection, acoustic or otherwise, taking place in proximity to a tidewater glacier must consider the safety and logistical challenges associated with working in a hazardous, actively calving zone. Operations must define a minimum safety distance to protect the people, vessel, and equipment; this distance is strongly dependent on a number of parameters unique to the glacial system being studied. Minimum safety distance definition and the subsequent impact on acoustic data collection and analysis are discussed in detail in Section 5.4.

4.3 Quantitative mixing analysis and geophysical parameter estimation

475

480

485

490

495

500

505

To characterize the tidally-driven mixing in Hansbukta, broadband acoustic observations were collected in tandem with measurements of dissipation rates, temperature variance (χ_T) and turbulent kinetic energy (ε) by the Epsi-fish in regions of stratified turbulence (Fig. 5). Comparison between broadband inversion measurements and the Epsi-fish ground truth dataset illustrates the potential for accurate, remote, acoustically derived measurements of dissipation rates in high-latitude regions. Furthermore, the high-resolution echograms collected by broadband echosounders systems can image and quantify the evolution of shear instabilities associated with mixing over large regions.

The broadband acoustic inversion method applied here has previously been leveraged to measure dissipation rates of turbulent kinetic energy in high energy systems with intense salinity gradients in the Connecticut River (160–600 kHz, Lavery et al., 2013). In highly turbulent strongly stratified water columns, backscattering can be driven by small, random perturbations in density and compressibility brought about by the fluctuations of the medium temperature and salinity associated with dynamic mixing (Goodman and Forbes 1990). A theoretical acoustic scattering model for isotropic homogenous turbulent microstructure (Lavery et al., 2003) is used here and is outlined in detail in Appendix 6.3. In short, the calibrated and corrected volumetric scattering derived from field observations is fit to the scattering model output, which is constrained by the in-situ data collected by the Epsi-fish, which was <150 m from the acoustic transect. Fitting the scattering model provides an acoustically derived measurement of the dissipation rate of TKE, ε .

The application of broadband acoustic inversion to remotely measure dissipation rate TKE was applied to the acoustic transect collected running from north to south into the main channel of Hornsund Fjord, the area of interest just outside the primary sill of Hansbukta (Fig. 1). The data were collected near the peak ebb tide and the echogram shows elevated scattering associated with shear instabilities, thermohaline structure, and individual fish in the region of interest highlighted in Fig. 5, between 10-and 28 meters depth. The vertical profiles of temperature and salinity from the coincident Epsi-fish cast show several pycnocline regions associated with glacially derived water mass, similar to the structure observed in Fig. 3 and discussed in Section 4.1. At the sharp thermocline at ~16 m depth, TKE and thermal dissipation rates observed from the Epsi-fish are

elevated more than an order of magnitude above background levels. Elevated scattering is seen at the same location, associated with shear instabilities that evolve along track into a breaking internal wave.

The dissipation rate of TKE can be measured from the backscattered signal with the help of a theoretical acoustic scattering model and direct sampling from the Epsi-fish. The Epsi-fish measurements not only inform the acoustic scattering model but were used to validate the acoustically derived measurements. The local temperature and salinity measured by the Epsi-fish (Fig. 5) were used to estimate the molecular kinematic viscosity (v), the saline contraction and thermal expansion coefficients $(\beta \text{ and } \alpha)$, the fractional change in sound speed due to temperature and salinity $(\underline{a} \text{ and } b)$, and the mean gradients of salinity $(\partial \overline{S}/\partial z)$ and temperature $(\partial \overline{T}/\partial z)$. Together with peak values of the dissipation rate of TKE (ε) , the Epsi-fish measurements were used to:

- 1) determine the turbulent energy regime of the broadband acoustic observations,
- 2) model the predicted frequency-dependent backscattering cross section (σ_v) and
- 3) validate our acoustically derived estimate of dissipation rate of TKE (ε).

510

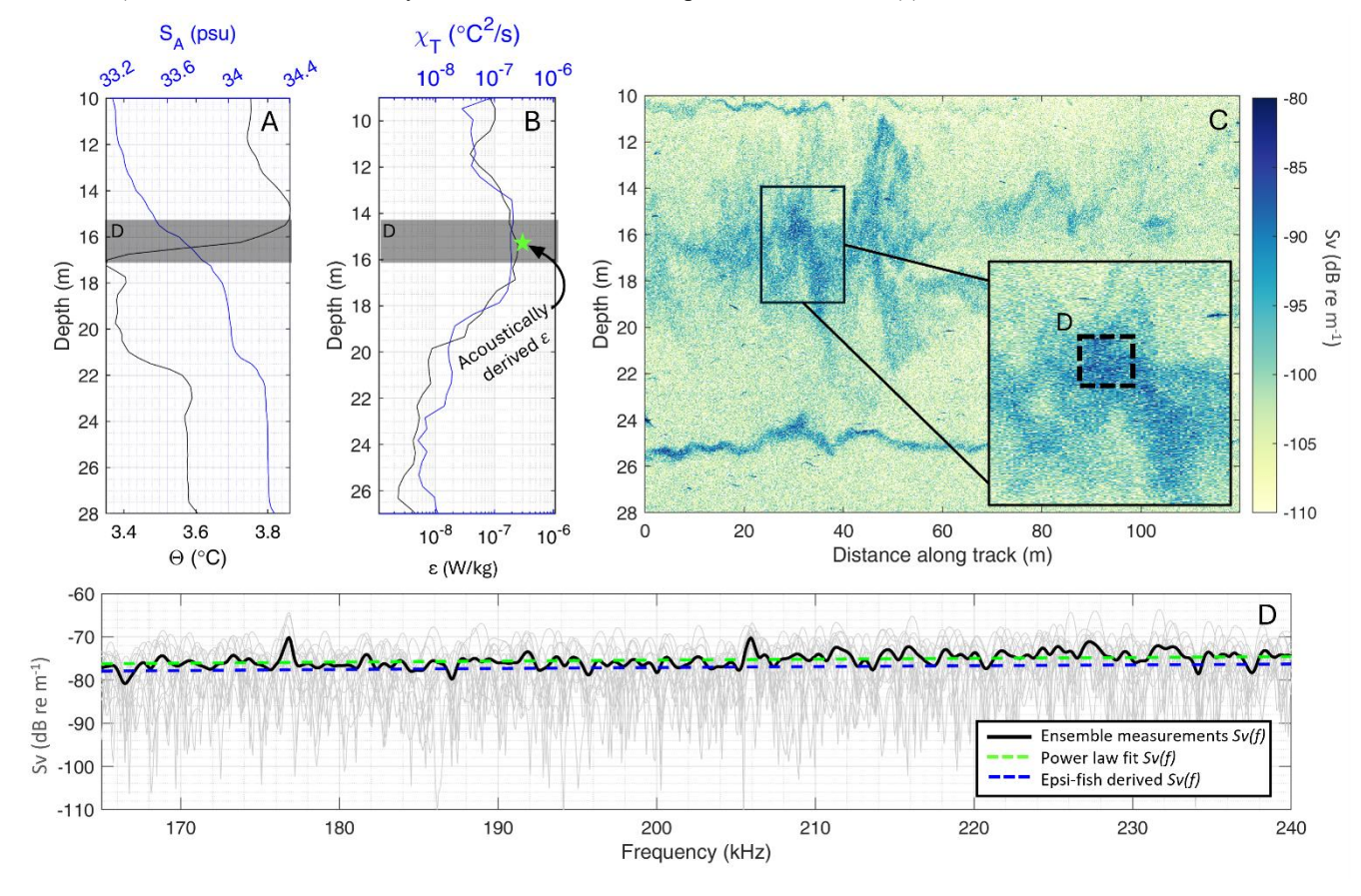


Figure 5: Combining Epsi-fish ground truth and broadband acoustic data to better characterize mixing in the water column. Vertical profiles of temperature and salinity (panel A), and dissipations rates of temperature variance and turbulent kinetic energy (panel B) measured by the Epsi-fish cast. Panel C is echogram of backscattering intensity (Sv) collected in close proximity (within 150 m) to the Epsi-fish cast. The inset box in C provides an enlarged view of the sampled region (dashed box marked D), from which Sv(f)

was calculated using Eq. (2) and is plotted in panel D. The light grey lines in panel D are the individual measurements of Sv(f) from each sampled acoustic record and the thick black line is the ensemble average of all records. The dashed green line is the power law fit of the ensemble Sv(f) measurement, which was used to invert for ε . The acoustically derived ε is plotted in panel B (green star). The dashed blue line in panel D is the output of Eq. (1) evaluated with the Epsi-fish direct measurements, taken from the regions highlighted with the dark box in panels A and B. See Fig. 1 (yellow highlighted transect lines and yellow marker) for transect and Epsi-fish profile locations within the larger study site of Hansbukta.

The Epsi-fish measurements of the region of interest in Fig. 5 indicate all the acoustic observations fell well within the viscousconvective turbulent energy regime. As a result, the scattered energy from the turbulent mixing associated with breaking internal wave, here referred to as the backscattering cross section (σ_v), could be computed following Eq. (6) from Lavery et al. (2013):

$$\sigma_{v}(f) = 2^{-3} f q \left(\frac{\varepsilon}{v}\right)^{-\frac{1}{2}} \frac{4\pi \varepsilon R_{F}}{cg\beta} \frac{\partial \bar{S}}{\partial z} \left(A^{2} \left(\frac{\partial \bar{T}/dz}{\partial \bar{S}/dz}\right)^{2} + B^{2} + 2AB \frac{\partial \bar{T}/dz}{\partial \bar{S}/dz}\right)$$
(1)

where f is the acoustic frequency in kHz, evaluated over the range 160-240 kHz, q is a constant defined by Oakey (1982), c is the speed of sound, R_f is the non-dimensional Richardson Flux number, defined by Osborn (1980) as 0.15, g is the gravitational constant, and A and B account for the fractional changes in sound speed and density due to temperature and salinity, such that $A=\alpha+a$ and $B=\beta-b$. The full derivation for Eq. (1) is found in Appendix C.

Equation (1) was used to predict the broadband backscattering intensity spectra over the experimental frequency range (160-240 kHz) using the Epsi-fish measurement (Fig. 5). The Epsi-fish derived predictions of backscattering cross section were then compared to acoustically derived measurements of backscattering cross section in the region of interest.

To compute $\sigma_v(f)$, a time series with a length of 36 samples, approximately 0.28 milliseconds, was extracted across 25 acoustic profiles. The Fourier transform of the profiles was taken to compute the frequency-dependent backscattering (S_{mf}). The ensemble average, backscattering cross section was computed from the ensemble of the extracted S_{mf} measurements following a modified form from Weber and Ward (2015):

$$\sigma_{v}(f) = \frac{\langle |s_{mf}(f)|^{2} \rangle}{c(f)} \frac{r^{4}}{exp(-4\alpha_{a}(f)r)} \frac{1}{V(f)}$$

$$\tag{2}$$

540

550

555

where the brackets $\langle \rangle$ specify an ensemble average over multiple acoustic profiles, C is the frequency-dependent main response axis (MRA) correction factor, r is the range to the region of interest, α_a is the frequency-dependent absorption coefficient in neper/meter, and V is the frequency-dependent ensonified area. The volumetric backscattering intensity, plotted in Fig. 5, is the logarithmic form of backscattering cross section, volumetric scattering, Sv, such that $Sv=10 \log_{10}(\sigma_v)$ with units of dB re 1/m. An in-depth discussion of Eq. (2) can be found in Appendix B.

The analysis of the acoustic measurements can be expanded upon. For example, the measurements of backscattering cross section can be inverted using Eq. (1) to directly, remotely estimate the dissipation rate of TKE. The model (Eq. (1)) was rewritten to solve for the dissipation rate of TKE using both the ensemble average volume scattering measurements and the basic oceanographic measurements from the Epsi-cast, and then evaluated to provide a remote, acoustically derived measurement of the dissipation rate of TKE which can be compared to the Epsi-fish in-situ measurement. This method is not

without precedent; it has been successfully applied in the Connecticut River by Lavery et al. (2013) and in the Baltic Sea by Muchowski et al. (2022).

560

565

570

575

580

Before discussing the results of the broadband measurements of frequency-dependent backscattering cross section and the resulting inversion estimating the dissipation rate of TKE, it is important to clarify the assumptions involved in this analysis. First, there is an approximately 150 m separation between the deployment location of the microstructure probe and the acoustic data shown in Fig. 5. Both data were taken approximately the same distance from the sill, but the measurements made by the Epsi-fish may not be representative of the water column sampled by the acoustic system, especially if mixing associated with the sill had spatial heterogeneity. Furthermore, the acoustic scattering model (Eq. (1)) used in this analysis assumes homogenous, isotropic turbulent microstructure is responsible for the scattered signal and any patchiness in that phenomenon is not accounted for in the model application. The short ranges associated with this analysis mean the area sampled is relatively small, <3 m³, and previous research (e.g., Muchowski et al., 2022), working in deeper conditions (larger sampled areas) have made the homogenous, isotropic assumption. Finally, the use of a single acoustic scattering model for inversion estimates assumes either a single or dominant scattering mechanism. It is always possible, indeed likely, that multiple scattering mechanisms are present in the sampled region at a given moment in time; however, this ambiguity can be broken by considering the broadband spectral response and comparing field measurements to the known frequency dependencies of various potential scattering mechanisms, as is done in the following paragraph.

There is excellent agreement between both the modeled predictions of volumetric scattering and the values of dissipation rate of TKE measured by the Epsi-fish cast and the acoustically derived observations as illustrated in Fig. 5. First, the acoustic field measurements of volume scattering from the region associated with the breaking internal wave show a weakly positive frequency dependence of f^t , measured by least-square fitting a power law distribution. This power law dependence is the same as that predicted by Eq. (1) for backscattering from turbulent microstructure in the viscous-convective regime. While there are indications of other scattering mechanisms in the echogram (e.g., fish, thermohaline structure), neither have this power law spectra dependency; this combined with Eq. (1) and the general context suggests that the elevated scattering observed associated with the region centered at 16 meters depth is driven by turbulent microstructure. Here, the dissipation rate of TKE derived through acoustic inversion was measured to be 5.5×10^{-7} (W/kg); compared to the peak Epsi-fish measurement of 2.7×10^{-7} (W/kg). The close agreement, within a factor of two, suggests that the acoustic method is viable, and that the backscattering signal observed in the echogram surrounding the region of interest could be inverted to provide estimates of the dissipation rate of TKE over a larger area, leveraging the high-resolution nature of acoustic data to characterize mixing across the region.

Future work will expand the acoustically derived measurements to contextualize dissipation rate variability at the sill over various stages in the tidal cycle and over the subglacial discharge plume in the glacial trough. The highly resolved nature of broadband echograms, defined by both individual acoustic profile depth resolution and the spacing of along-track profiles, means we can extract measurements of dissipation rates at spatial scales unheard of with direct profile sampling equipment

and use these high-resolution measurements to better inform mixing models in the highly dynamic high-latitude fjords; such information can improve our understanding of heat and salt transport across fjords. The fact that TKE dissipation rates that can be obtained remotely is going to be a critical tool for understanding ablation mechanisms at the glacier terminus, where it is very difficult to obtain in-situ measurements.

5 Considerations in the use of broadband active acoustic tools

590

595

600

605

610

Despite their many strengths, broadband acoustic systems are not generally used as a stand-alone observational tool and the successful collection of quality data depends on thorough and well-defined mobilization, deployment, survey procedures, field processing and data quality control and assessment methods. First, while split-beam transducers have straightforward deployment geometries and minimal positioning and motion data stream requirements in comparison to other types of active acoustic systems (e.g., multibeam echosounders), broadband transceivers are sensitive to external noise sources (e.g., other active acoustic systems, ship noise, electrical interference). The successful collection of quality broadband water column data requires a well-considered mobilization plan for field activities, discussed in Section 5.1. Second, quantitative analysis, such as broadband spectral characterization or acoustic inversion procedures, requires calibration of the echosounder and application of a series of corrections related to sound propagation and scattering. The post-processing pipeline for broadband data to account for these corrections remains a barrier for new users. Many research groups rely on processing tools developed inhouse because of the lack of open-source commercial software. Techniques for processing are improving; several open-source data analysis tools have become available in recent years, such as EPS3 (Ladroit and et al., 2023) and EchoPype (Lee et al., 2021). Commercial developers have tools to process narrowband data and have recently started to expand processing capability to broadband systems. However, these software packages are costly and their broadband spectral analysis tools are still in the early stages of development. Section 5.2 covers the needs to account for the underlying physics of sound propagation and the budget of time and personnel for these activities during field expeditions. The inherent ambiguity in acoustic observations briefly noted in Section 4 and the ongoing challenge in interpreting all active acoustic data, no matter the quality of data collection is discussed in Section 5.3. Finally, in Section 5.4 there is a discussion of safety, data collection, and data quality considerations that come into play when making observations in proximity to the terminus of a tidewater glacier.

5.1 Noise considerations during deployment

Echosounders used in scientific applications have high receive sensitivity, which allows for the measurement of a wide frequency range of relatively low amplitude acoustic signals. High receive sensitivity, combined with pulse compression signal processing, enables the observation of weakly scattering phenomenon, such as thermohaline and mixing structure, as reported in Fig. 3-5; however, high receive sensitivity also makes broadband echosounders susceptible to external noise across a broad range of frequencies, from other acoustic systems (e.g., ship bottom pingers), environmental sources (e.g., wind, waves), ship noise, and electrical interference. From a practical perspective, any increase in interference to the received acoustic signal from

external noise sources will reduce the signal-to-noise ratio of the system, which results in a reduction of the range of detection of objects in the water column and broadband spectral characterization capabilities.

Vessel mobilization of the broadband transducers must consider equipment placement with respect to noise sources and flow structures, as well as transducer safety, to ensure the collection of quality data. Electrical noise, often caused by electromagnetic interference from ship-based power or voltage drops from high-current equipment, such as winches, commonly reduces the quality of acoustic data. Noise reduction measures must also be considered in the installation and acquisition procedures of the acoustic topside unit. When the EK80 wideband transceiver was acquiring acoustic data during the Hornsund fiord expedition the MV Ulla Rinman's ship sonar was turned off to remove potential for crosstalk between the two systems. During collection of in-situ data the broadband system did not acquire data, due to interference from the ship's winch and at the completion of in-situ data collection the winch and all associated electronics were secured. Furthermore, the full suite of broadband echosounder equipment (e.g., transducer, transceiver, positioning system, acquisition laptop) was run from a separate marinegrade battery, due to electrical noise associated with ship power. Furthermore, the ES200-7CD split-beam transducer was deployed from a side-mounted pole on the forward, starboard side of MV Ulla Rinman. The side-mounted pole was a total of 6 meters in length, with 2 meters sitting below the water line to protect the transducer from interaction with surface ice mélange. The location of the pole was selected to minimize vibrations and the impacts of bubbles entrained by the vessel to help minimize noise and performance degradation. Additionally, the pole location on MV Ulla Rinman also allowed the field team to maintain visual contact during survey activities from the ship's bridge, as well as easy access for regular pole deployment and acoustic calibration procedures. Installation of the transducer must ensure as close to a laminar waterflow over the transducer face as possible, as any vibration will be converted into electrical energy, contributing to the background noise level.

5.2 Acoustic corrections in post-processing

625

630

635

640

645

650

The successful interpretation of acoustic data relies upon the accurate and thoughtful application of corrections in the post-processing pipeline. Appropriate corrections are dependent on the type of analysis but typically include the application of a calibration offset to account for the accuracy and precision in signal transduction and measurements, geometric spreading corrections, and frequency-dependent absorption estimations, see Eq. (2).

Acoustic instruments need to be calibrated frequently, as their performance will change with the deployment environment and over the life of the instrument (Demer and Hewitt, 1993; Brierley et al., 1998; Nam et al., 2007). It is best practice to calibrate as system over the range of environmental conditions encountered when measurements are made; water temperature is of particular concern for high-latitude work. Calibration methods for split-beam echosounders are well defined in the literature and are described in detail in Demer et al. (2015). In short, a small (<50 mm) sphere of known physical properties is hung in the beam of the acoustic transducer on the experiment platform and moved throughout the acoustic beam, where its position is determined through split-aperture processing to measure variability in sensitivity. The expected backscattering from the sphere is calculated using a theoretical model for the reflection of sound by elastic spheres (MacLennan, 1981) and is compared

to the measurements made in the field. The resulting calibration offset, for example C(f) in Eq. (A2), adjusts the gain and filter attenuation correction factor of echosounder measurements, as well as corrects for frequency-dependent beamwidth and receive sensitivity inherent to broadband echosounders (Rogers and Van Buren, 1978).

Beyond calibration offsets, all quantitative acoustic analysis must account for the frequency-dependent absorption of acoustic energy by the propagation medium and the geometric spreading of the acoustic signal. Acoustic absorption refers to the gradual loss of energy due to interaction with water molecules and dissolved substances. Absorption is a function of both seawater properties (e.g., temperature, salinity), as well as frequency and is corrected for in logarithmic space for frequencies between 160-240 kHz in dB/m (Francois and Garrison, 1982). Geometric spreading refers to the propagation of the broadband signal outward in all directions from the transducer resulting in a range-dependent loss of acoustic energy for a given area. Depending on the underlying physics of the scattering phenomena in question, geometric spreading can be accounted for with different range-dependent corrections, the most common being spherical spreading correction, but other corrections may be more appropriate depending on circumstances.

5.3 Ambiguity in the backscattered signal

Observations made by active acoustic systems are inherently ambiguous, as scattering in the water column can be associated with multiple dynamics and visually differentiating between processes is not always possible. The correct interpretation of backscattering signals requires an understanding of how acoustic systems work and proper application of corrections for sound propagation and scattering associated with targets, like those discussed in Section 5.2. In circumstances where these steps are skipped, the potential for inaccurately identifying water column processes and mis-quantifying geophysical parameters is high. As discussed in Section 4.3, broadband spectral analysis combined with theoretical acoustic scattering models can differentiate between scattering mechanisms; however, direct measurements remain an essential and straightforward tool to inform and contextualize remote acoustic observations. Field procedures should plan to include co-located in-situ sampling when possible; these data can provide context and clarity to the acoustic observations, as illustrated in Section 4.1, as well as inform theorical acoustic scattering models to assist in broadband spectral analysis, as in Section 4.3.

The application of acoustic scattering models to explain broadband spectral characteristics or assist in acoustic inversion methods also requires forethought and experience. Many broadband inversion methods have been developed to apply to cases in which one scattering mechanism dominates the ensonified volume, e.g., sizing gas bubbles (Weidner et al., 2019), estimating rates of TKE dissipation in a highly stratified estuary (Lavery et al., 2013). In these cases, acoustic inversion procedures are constrained by the nature of the sampled volume, as well as the number of free parameters in the theoretical acoustic scattering model and the quality of the in-situ sampling. Water column scattering is often associated with multiple dynamics, i.e., entrained gas bubbles associated with regions of intense mixing (Marston et al., 2023). When there is no dominant scatterer in the ensonified volume, inversion efforts are limited by the unknown combination scattering from multiple phenomena and the under-sampled nature of the inversion problem. Such issues can be overcome with knowledge of the study site, quality ground truth data, and well-defined theoretical acoustic scattering models (e.g., Loranger et al., 2022; Lavery et al., 2010).

All considerations combined, users of broadband split-beam echosounders should be prepared to refine deployment methodologies and employ noise reduction procedures to ensure the collection of high-quality acoustic data. Upon field work completion users should take the time to properly calibrate and correct data prior to analysis. Finally, users should carefully select and apply theoretical acoustic scattering models based on the best knowledge of data and model limitations for accurate and meaningful results.

5.4 Safety considerations near glacial termini

690

695

700

705

710

715

Calving events, above and below the waterline, create a dangerous environment in proximity to the ice-ocean interface of tidewater glaciers. Falling or surfacing ice and the resulting surface waves pose serious dangers near the calving front. As noted earlier, there is a paucity of observations in this region due to safety concerns, which preclude direct, ship-based sampling (e.g., deployment of sensors, water sampling). In Section 4.2 we discussed the use of broadband scientific echosounders to fill observational gaps by making remote measurements of this region, using as an example data collected at Hansbreen. However, the broader deployment of scientific echosounders for the study of submerged glacial termini and the proximal water column requires several important safety considerations, which in turn have implications for data collection and quality. Ship-based acoustic measurements of the ice-ocean interface must be made at a minimum safe distance (MSD) from the calving front. The MSD will vary glacier-to-glacier but is generally ~200 m and accounts for the height of the ice cliff above the water line, the fjord topography and bathymetry, and the calving rate (Koher, 2009). In fjords that are narrow or shallow, or have ice cliffs higher than 40-50 m, the MSD can be upwards of 500 m or more.

An extended MSD can impact the successful use of scientific echosounders for high latitude studies and must be considered prior to field operations. The broadband transducer highlighted in this paper, the Simrad ES200-7CD, has a maximum useable range of approximately 250 m, beyond which signal attenuation reduces the signal to noise ratio below useable levels. However, signal attenuation is primarily driven by the frequency of the acoustic pulse and several lower frequency system could be used to extend the data collection range to beyond 700 m. Increased distance between the acoustic transducer and the ice face also results in an increased observational area, defined by the acoustic beam footprint (e.g., the transducer beamwidth). An increased acoustic footprint limits the study of closely spaced phenomenon, such as individual bubbles, fish, or small-scale surface roughness of the ice face, but allows for a larger observational area.

Overall, the feasibility of deploying broadband scientific echosounders for the study of the ice-ocean interface of tidewater glaciers will be highly dependent on the glacier in question. Deploying a high frequency (>200 kHz) scientific echosounder on an operator run vessel may not be feasible in cases where the MSD is large (>200 m). In such cases, other deployment platforms could be considered, such as uncrewed surface vehicle (USV) which can reduced the range between the transducer and submerged ice face. However, it is worth noting that integration of an acoustic system onto an USV can be complicated and will increase the cost of the deployment beyond what has been quoted in this paper.

6 Conclusions

720

725

730

735

740

745

Broadband split-beam scientific echosounders are a remote sensing tool particularly well suited for field deployment in highlatitude fjords. The high rate of acoustic profile collection and resulting data resolution is unmatched in comparison to traditional direct sampling. Broadband echograms provide illumination of the evolution of numerous scattering phenomena in the water column, including shear instabilities associated with bathymetry and tidally forced mixing, biological scattering from fish aggregations, and evolving thermohaline structure. As illustrated in this manuscript, these observations can be used to contextualize water column dynamics over the full fjord scale, remotely characterize processes occurring in dangerous or inaccessible locations (e.g., the submerged terminus), and provide geophysical measurements of water column processes through broadband spectral inversion when combined with *in-situ* sampling and theoretical scattering models. Looking beyond the analysis discussed in this work, broadband split-beam systems have a history in the study of bio-physical interactions (e.g., Benoit-Bird et al., 2009; Lavery et al., 2010), seafloor emission characterization (e.g., Loranger and Weber, 2021; Weidner et al., 2019), and sea ice (Bassett et al., 2020). The prospects for future studies of high-latitude glacial fjords with broadband systems are excellent, as they can improve observational capabilities in isolated and challenging field locations through the collection of qualitative images and quantitative measurements.

Tracking the spatiotemporal variability of fjord-scale thermohaline structure and quantifying dissipation rates will help characterize the relative importance of tidal forcing on heat, salt and freshwater budgets in the highly dynamic high-latitude fjords like Hornsund fjord. Concurrently, at the terminus of Hansbreen, split-aperture processing techniques have been employed to precisely determine the position and morphology of the submerged ice face (Weidner, 2025). These measurements will be combined with terrestrial laser scans to explore calving regimes above and below the waterline at Hansbreen.

Broadband echosounders are available to the oceanographic community from commercial sources. The start-up cost is approximately \$80,000 USD (78,000€ EUR) for the transducer, transceiver, and license to operate, and many systems are portable, with flexible deployment geometries and mobilization needs, making them an appealing tool for field work when time and space is limited (e.g., Cade et al., 2022). Furthermore, many research vessels, including those operating in polar regions, are already equipped with split-beam narrowband sonar systems that can be upgraded with broadband capability at minimal cost. The application of broadband echo sounders in polar regions could thus enable an improved understanding of the complex geophysical dynamics of high latitude fjords.

7 Appendix A: Equipment field mobilization and data collection procedures

Mobilization and calibration of the broadband acoustic system and other sampling equipment on MV Ulla Rinman took place on July 5-6, 2023. The acoustic system was operated continuously during survey operations in broadband mode. The transmit power was set to 150 W, and the pulse length was set to 1.012 ms. During mobilization, the acoustic system was calibrated with a 25 mm tungsten-carbide sphere following the well-documented procedure from Demer et al. (2015) in the western channel of Burgerbukta in Hornsund Fjord. The location was protected from swell and winds in the main channel of Hornsund

fjord and was calm and ice-free during calibration operations. A CTD cast was taken prior to calibration to characterize the water column properties. Field calibration results were compared to a post-expedition laboratory calibration which took place in the engineering tank at the University of New Hampshire on March 13, 2024, with the same acoustic equipment. Beam pattern characterization and broadband spectral power calibration results from the field and lab agreed, confirming the health of the transducer and calibration offset values applied in post-processing.

750

765

770

780

The Valeport miniCTD unit and the Epsi-fish microstructure probe were used for *in-situ* water column sampling and were mobilized on July 6th, 2023. The miniCTD unit was deployed from the starboard aft of MV Ulla Rinman on the upper level via the ship's winch. The winch provided a downward velocity of approximately 30 cm/s. The mini CTD sensor went through a 30 second initialization procedure at 1 m depth prior to the cast. The Epsi-fish was deployed from the starboard aft of MV Ulla Rinman via a commercial fishing reel with a controlled descent rate of ~0.6 m s⁻¹. Time lapse imagery was collected with two GoPro Hero11, which were deployed from the bridge deck and the transducer pole off the starboard side.

Acoustic survey activities took place between July 7 and 12, 2023 and consisted of approximately 80 km of broadband acoustic water column data, 40 CTD profiles, and 7 microstructure casts. During acoustic survey work, MV Ulla Rinman vessel speed was limited to between 2-3 knots (~1-1.5 m/s), to maintain acoustic data density. Acoustic system parameters and direct sampling deployment procedures were kept consistent throughout survey activities.

The downward-looking geometry was employed to collect a series of north-south transects. The north-south transects were approximately 5 km long. All transects were run in pairs. The first transect was run continuously from the mouth of Hansbukta to the terminus of Hansbreen, collecting broadband acoustic data only. This provided continuous, uninterrupted acoustic observations of water column dynamics at the full-fjord scale. The second transect was run in the reciprocal direction, acoustic data was collected, interspersed with ground truth data collection at specific locations: near the terminus of Hansbreen, in the glacial trough before the first set of sills, at the terminal moraine (shallowest sill), and in the main channel on Hornsund fjord at the mouth of Hansbukta. North-south transects, along with ground truth measurements, were collected in Hansbukta during multiple sections of the tidal cycle to capture the potential effect of tidal influence on mixing across the fjord. The tides in Hornsund fjord are semi-diurnal, with two low- and high-tides of approximately equal magnitude and total tidal range generally between 2-3 m. Transect timing was determined using predicted tidal data from the Longyearbyen tidal station. In post processing, tidal phase was determined from sea surface height measured by a pressure sensor from a mooring deployed in Hansbukta during survey operations.

The side-looking geometry was utilized to scan the ice-ocean interface of Hansbreen and remotely characterize processes occurring at the terminus. The geometry of the transducer mount set-up provided a tilted beam geometry to collect observations of the near-terminus water column and the ice-ocean interface along a diagonal trajectory. The acoustic beam intersected with the submerged terminus between 15-25 m below the surface, depending on the distance between the ship and the ice face, which was not more than 200 m. The area ensonified was between 2.5 to 8.5 m². Survey lines were run from east to west, as the side-mount pole was on the starboard side of MV Ulla Rinman. During the survey there was minimal ice mélange, which allowed for the same parallel track to be run several times. Parallel transects included the collection of CTD profiles and time

lapse photos. The CTD profile locations were chosen based on the subglacial discharge plume location, as observed in the acoustic data.

8 Appendix B: General flow of acoustic processing

785

790

795

800

805

810

All acoustic data presented in this manuscript are plotted as volume backscattering intensity, Sv, which has logarithmic units of decibels relative to I/m and is computed as $Sv = 10 \log_{10} \sigma_v$, defined below in Eq. (A1) to (A4). Volume backscattering intensity is a measure of the distributed scattering strength normalized by acoustic beam volume, which increases with increasing range from the transducer. The computation of Sv has the following steps: 1) application of the matched-filter, 2) sampling of the acoustic time series, 3) range dependent corrections for signal attenuation from spherical spreading and absorption, 4) calibration offset and beam volume correction application, and 5) corrections for vessel motion. Steps 1-4 are described in greater detail below.

Sv computation is based on well-defined matched-filter processing procedures (e.g., Weber and Ward, 2015; Lavery et al., 2017; Andersen et al., 2024) and for this manuscript is calculated by modifying seafloor scattering intensity, $\sigma(f)$, from Weber and Ward (2015), starting with Eq. (9):

$$\sigma(f) = \langle |S(f)|^2 \rangle \frac{1}{C(f)} \frac{r^4}{\exp(-4\alpha(f)r)} \frac{1}{A}.$$
(A1)

Eq. (A1) reports scattering by the statistics of an ensemble of realizations, $\langle \cdot \rangle$, of individual seafloor scattering observations, $|S|^2$. The C in the second term is the main response axis (MRA) correction factor. The third term represents a combination of spherical spreading losses and absorption, where a is the frequency-dependant absorption coefficient in units of nepers/m and r is the range between the region of interest in meters and the transmitter/receiver. Finally, scattering is corrected for the ensonified area of the seafloor in question, A in m^2 .

In this manuscript, Eq. (A1) is modified to consider a region of scattering from a volume in the water column, rather than an area on the seafloor, resulting in measurements of volume backscattering intensity, Sv. The ensemble realizations of scattering observations and corrections from the second and third terms of Eq. (A1) remain the same; however, the fourth term becomes a correction for beam volume, rather than area. For broadband spectra analysis (Section 4.3, Fig. 5), the modified equation takes the form:

$$\sigma_{v}(f) = \frac{\langle |S_{mf}(f)|^{2} \rangle}{c(f)} \frac{r^{4}}{\exp(-4\alpha(f)r)} \frac{1}{V(f)}$$
(A2)

where terms have the same definitions as Eq. (A1), except V which is the frequency-dependent ensonified area. The frequency-dependent scattering of water column observations, $S_{mf}(f)$ is computed from the Fourier Transform of the base-banded, matched-filtered output (s_{MF}) . The matched-filter enhances the resolution and detection of water column targets and maximizes the signal-to-noise ratio (SNR). s_{MF} is computed from the summed signal from all four quadrants of the split-beam transducer, s(t) and an idealized transmit pulse, $s_I(t)$

$$s_{MF}(t) = \frac{s(t) \otimes s_I(t)^*}{|s_I(t)|^2} \tag{A3}$$

The frequency-dependent ensonified volume can be approximated as a cylinder (see Fig. 3.17 in Lurton, 2010) defined by the range from the transducer to the region of interest, and the two-way equivalent beam angle. *V* can be calculated using the following (Eq. 3.44 Lurton, 2010):

$$V(f) = \Psi(f)r^2 \frac{cT}{2} \tag{A4}$$

where T is the length in seconds of the analysis window, r is the range to the center of the region of interest (c(t - T/2)/2), c is the speed of sound, and $\Psi(f)$ is the frequency-dependent two-way equivalent beam angle (in steradians), as defined in 320 Jech et al., (2005):

$$\Psi(f) = \int_{-\pi}^{\pi} \int_{0}^{\pi} b_{t}(\theta, \phi) b_{r}(\theta, \phi) \sin \theta \, d\theta \, d\phi \tag{A5}$$

where b_t and b_r are the acoustic transmitter and receiver beam pattern respectively, and θ and ϕ are polar spherical coordinates.

To produce high-resolution echograms (Section 4.1-4.2, Fig. 3, 4), we consider volume backscattering intensity in the time domain, rather than the frequency domain and σ_v is defined as

$$\sigma_{v}(t) = \frac{|s_{mf}(t)|^{2}}{C} \frac{r^{4}}{\exp(-4\alpha r)} \frac{1}{V}.$$
(A6)

where corrections for absorption and main response axis (MRA) correction factor are evaluated at nominal center frequency of the transducer, 200 kHz, and the time-domain matched-filtered output (s_{MF}) from Eq. (3) is used directly to compute σ_v . In the time domain, the ensonified volume can be approximated as a cylinder defined by the range from the transducer to the region of interest and the -3dB beam angle (θ_{3dB}) provided by the manufacturer

$$V = \tan(\theta_{3dB}) \, r \frac{\epsilon \tau_{eff}}{2} \tag{A7}$$

where τ_{eff} is the effective pulse length in seconds. Eq. (A4) can also be used to compute the ensonified volume for a time-domain correction by modifying Eq. (A5) to compute the two-way equivalent beam angle at the nominal center frequency of the transducer.

For additional information on acoustic data processing steps and the computation of volumetric scattering intensity, we refer readers to Lavery et al. (2017) and Andersen et al. (2024) for alternative derivation and formulations of Eq. (A2) and (A6), as well as additional explanation of broadband acoustic signal processing and calibration corrections.

9 Appendix C: Theoretical acoustic scattering model for turbulent microstructure

830

The wavenumber spectra for temperature and salinity are separated into three wavenumber regimes in the isotropic, homogenous turbulence model from Bachelor (1959). The measurements made in Hornsund Fjord with the ES200-7CD echosounder are limited to the viscous-convective subrange. In the viscous-convective regime, the 1D wavenumber spectra for temperature are given by Lavery et al., 2013, Eq. (2)

$$\phi_{T,S} = q \chi_{T,S} \left(\frac{\varepsilon}{n}\right)^{-1} k^{-1} \tag{A8}$$

and their co-spectra is given by:

845
$$\phi_{T-S} = q(\chi_T \chi_S)^{\frac{1}{2}} \left(\frac{\varepsilon}{\nu}\right)^{-\frac{1}{2}} k^{-1}$$
 (A9)

where k is the wavenumber (m^{-1}) , q is a dimensionless constant, defined by Oakey (1982) at q = 3.7, $\chi_{T,S}$ are the dissipation rates of temperature and salinity variance $({}^{\circ}C^2/s, PSU^2/s)$, v is the molecular viscosity (m^2/s) , and ε is the dissipation rate of TKE (W/kg).

The scattering cross section per unit volume from homogeneous and isotropic fluctuations in temperature and salinity is given by Lavery et al. 2003 (Eq. 23) as

$$\sigma_{v}(k) = -\frac{k^{4}}{k} \left(A^{2} \frac{\partial \phi_{T}(K)}{\partial k} + B^{2} \frac{\partial \phi_{S}(K)}{\partial k} + 2AB \frac{\partial \phi_{T-S}(K)}{\partial k} \right) \tag{A10}$$

A and B are terms that represent the fractional change in sound speed and density due to temperature and salinity changes. For the backscattering case in this manuscript, the wavenumber spectra in A9 are evaluated at the Bragg wavenumber (K = 2k).

$$\sigma_{\nu}(k) = 2^{-3}kq \left(\frac{\varepsilon}{\nu}\right)^{-\frac{1}{2}} \left(A^{2}\chi_{T} + B^{2}\chi_{S} + 2AB(\chi_{T}\chi_{S})^{\frac{1}{2}}\right)$$
(A11)

The final expression for backscattering cross section per unit volume is derived by assuming the dissipation rates of temperature and salinity are related to the mean gradients in water column properties,

$$\chi_S = \chi_T \left(\frac{\partial \bar{S}}{\partial \bar{\tau}}\right)^2 \tag{A12}$$

and the dissipation rates of salinity and TKE can be related through the Richardson flux number (R_F) given by

$$R_F = \frac{g\beta}{2\varepsilon \gamma_c} \left(\frac{\partial \bar{S}}{\partial z}\right)^{-1} \tag{A13}$$

where β is the fractional change to density from salinity. Eq. (A12) and Eq. (A13) are plugged into Eq. (A11) to provide the following expression for σ_n

$$\sigma_{v}(k) = 2^{-3}kq \left(\frac{\varepsilon}{v}\right)^{-\frac{1}{2}} \frac{2\varepsilon R_{F}}{aB} \frac{\partial \bar{S}}{\partial z} \left(A^{2} \left(\frac{\partial \bar{T}}{\partial \bar{S}}\right)^{2} + B^{2} + 2AB \frac{\partial \bar{T}}{\partial \bar{S}}\right) \tag{A14}$$

which is used in the analysis to match the broadband spectral measurements of the breaking internal wave.

Data availability

The data that support this manuscript are available at https://doi.org/10.6075/J0N87B1B as part of the University of California San Diego Library Digital Collections. Information on the Polish Polar Station Hornsund can be found at https://hornsund.igf.edu.pl/.

Author contributions

EW and GD designed the acoustic field campaign. EW, GD, DS, HJ, HV, MC, and OG collected the dataset in Hornsund fjord.

EW analysed the data with assistance from GD, AB, MF, and FS. EW prepared the manuscript with contributions from all coauthors.

Competing interests

The authors declare that they have no conflict of interest.

Acknowledgements

The authors thank the captain and crew of MV Ulla Rinman and the staff of the Polish Polar Station in Hornsund Fjord for making the field expedition possible. Thank you to Carlo Lanzoni at the Center for Coastal and Ocean Mapping for calibrating the acoustic equipment. We also thank Larry Mayer and Anthony Lyons at the University of New Hampshire for the loan of the broadband acoustic system used in this work. Research efforts were supported by the Office of Naval Research, Award No. N00014-23-1-2620, N00014-21-1-2304, and N00014-21-1-2316. Weidner was supported in this effort by the Scripps Institution of Oceanography postdoctoral fellowship. Vishnu and Chitre were supported by the INTERACT III Transnational Access grant under the European Union H2020 Grant Agreement No.871120. Glowacki was supported by the National Science Centre, Poland grant no. 2021/43/D/ST10/00616. We also thank three anonymous reviewers for their comments which improved the content and readability of this manuscript.

References

- Abib, N., Sutherland, D.A., Amundson, J.M., Duncan, D., Eidam, E.F., Jackson, R.H., Kienholz, C., Morlighem, M., Motyka, R.J., Nash, J.D., Ovall, B., Pettit, E.C., 2023. Persistent overcut regions dominate the terminus morphology of a rapidly melting tidewater glacier. Annals of Glaciology 64, 1–12. https://doi.org/10.1017/aog.2023.38
 - Abib, N., Sutherland, D.A., Peterson, R., Catania, G., Nash, J.D., Shroyer, E.L., Stearns, L.A., Bartholomaus, T.C., 2024. Ice melange melt drives changes in observed water column stratification at a tidewater glacier in Greenland. EGUsphere 1–21. https://doi.org/10.5194/egusphere-2024-504
 - Amiri-Simkooei, A.R., Snellen, M., Simons, D.G., 2011. Principal Component Analysis of Single-Beam Echo-Sounder Signal Features for Seafloor Classification. IEEE Journal of Oceanic Engineering 36, 259–272. https://doi.org/10.1109/JOE.2011.2122630

- Andersen, L.N., Chu, D., Handegard, N.O., Heimvoll, H., Korneliussen, R., Macaulay, G.J, Ona, E., Patel, R., Pedersen, G., 2024. Quantitative processing of broadband data as implemented in a scientific split-beam echosounder, Methods in Ecology and Evolution, 15: 317-328. https://doi.org/10.1111/2041-210X.14261
 - Bamber, J., van den Broeke, M., Ettema, J., Lenaerts, J., Rignot, E., 2012. Recent large increases in freshwater fluxes from Greenland into the North Atlantic. Geophysical Research Letters 39. https://doi.org/10.1029/2012GL052552
- Bamber, J.L., Westaway, R.M., Marzeion, B., Wouters, B., 2018. The land ice contribution to sea level during the satellite era.

 Environ. Res. Lett. 13, 063008. https://doi.org/10.1088/1748-9326/aac2f0
 - Bassett, C., Lavery A.C., Lyons, A.P., Wilkinson, J.P., Maksym, T., 2020. Direct inference of first-year sea ice thickness using broadband acoustic backscattering. J. Acoust. Soc. Am. 147, 824–838. https://doi.org/10.1121/10.0000619
 - Bassett, C., Lavery, A.C., Ralston, D., Geyer, W.R., Jurisa, J.T., Thomson, J., Honegger, D.A., Simpson, A., Scully, M.E., Haller, M.C., 2023. Acoustic backscattering at a tidal intrusion front. Progress in Oceanography, 219. https://doi.org/10.1016/j.pocean.2023.103167.

- Beaird, N.L., Straneo, F., Le Bras, I., Pickart, R., Jenkins, W.J., 2023. Glacial Meltwater in the Current System of Southern Greenland. Journal of Geophysical Research: Oceans 128, e2023JC019658. https://doi.org/10.1029/2023JC019658
- Bemis, K., Lowell, R.P., Farough, A., 2012. Diffuse Flow: On and Around Hydrothermal Vents at Mid-Ocean Ridges. Oceanography 25, 182–191.
- 910 Bendtsen, J., Mortensen, J., Lennert, K., Rysgaard, S., 2015. Heat sources for glacial ice melt in a west Greenland tidewater outlet glacier fjord: The role of subglacial freshwater discharge. Geophysical Research Letters 42, 4089–4095. https://doi.org/10.1002/2015GL063846
 - Benoit-Bird, K.J., Cowles, T.J., Wingard, C.E., 2009. Edge gradients provide evidence of ecological interactions in planktonic thin layers. Limnology and Oceanography 54, 1382–1392. https://doi.org/10.4319/lo.2009.54.4.1382
- 915 Björk, G., Jakobsson, M., Assmann, K., Andersson, L.G., Nilsson, J., Stranne, C., Mayer, L., 2018. Bathymetry and oceanic flow structure at two deep passages crossing the Lomonosov Ridge. Ocean Science 14, 1–13. https://doi.org/10.5194/os-14-1-2018
 - Błaszczyk, M., Ignatiuk, D., Grabiec, M., Kolondra, L., Laska, M., Decaux, L., Jania, J., Berthier, E., Luks, B., Barzycka, B., Czapla, M., 2019. Quality Assessment and Glaciological Applications of Digital Elevation Models Derived from Space-
- Borne and Aerial Images over Two Tidewater Glaciers of Southern Spitsbergen. Remote Sensing 11, 1121. https://doi.org/10.3390/rs11091121
 - Błaszczyk, M., Jania, J.A., Ciepły, M., Grabiec, M., Ignatiuk, D., Kolondra, L., Kruss, A., Luks, B., Moskalik, M., Pastusiak, T., Strzelewicz, A., Walczowski, W., Wawrzyniak, T., 2021. Factors Controlling Terminus Position of Hansbreen, a Tidewater Glacier in Svalbard. Journal of Geophysical Research: Earth Surface 126, e2020JF005763. https://doi.org/10.1029/2020JF005763
 - Błaszczyk, M., Jania, J.A., Kolondra, L., 2013. Fluctuations of tidewater glaciers in Hornsund Fjord (Southern Svalbard) since the beginning of the 20th century. Polish Polar Research 34, 327–352. https://doi.org/10.2478/popore-2013-0024

Błaszczyk, M., Moskalik, M., Grabiec, M., Jania, J., Walczowski, W., Wawrzyniak, T., Strzelewicz, A., Malnes, E., Lauknes, T.R., Pfeffer, W., 2023. The Response of Tidewater Glacier Termini Positions in Hornsund (Svalbard) to Climate Forcing, 1992-2020. Journal of Geophysical Research: Earth Surface 128. https://doi.org/10.1029/2022JF006911

- Blomberg, A.E.A., Weber, T.C., Austeng, A., 2018. Improved Visualization of Hydroacoustic Plumes Using the Split-Beam Aperture Coherence. Sensors 18, 2033. https://doi.org/10.3390/s18072033
- Böning, C.W., Behrens, E., Biastoch, A., Getzlaff, K., Bamber, J.L., 2016. Emerging impact of Greenland meltwater on deepwater formation in the North Atlantic Ocean. Nature Geosci 9, 523–527. https://doi.org/10.1038/ngeo2740
- 935 Bourke, R.H., Garrett, R.P., 1987. Sea ice thickness distribution in the Arctic Ocean. Cold Regions Science and Technology 13, 259–280. https://doi.org/10.1016/0165-232X(87)90007-3
 - Brierley, A. S., Goss, C., Watkins, J. L., and Woodroffe, P. 1998 a. Variations in echosounder calibration with temperature, and some possible implications for acoustic surveys of krill biomass. CCAMLR Science, 5: 276–281.
 - Burdic, W. S., 1991. Underwater Acoustic System Analysis, 2nd ed., pp. 328-331, Prentice Hall, Upper Saddle River, N. J.
- Ochauché, N., Hubbard, A., Gascard, J.-C., Box, J.E., Bates, R., Koppes, M., Sole, A., Christoffersen, P., Patton, H., 2014. Iceocean interaction and calving front morphology at two west Greenland tidewater outlet glaciers. The Cryosphere 8, 1457–1468. https://doi.org/10.5194/tc-8-1457-2014
 - Chu, D., Stanton, T.K., 1998. Application of pulse compression techniques to broadband acoustic scattering by live individual zooplankton. The Journal of the Acoustical Society of America 104, 39–55. https://doi.org/10.1121/1.424056
- Otter, E., Bassett, C., Lavery, A., 2021. Classification of broadband target spectra in the mesopelagic using physics-informed machine learning. The Journal of the Acoustical Society of America 149, 3889–3901. https://doi.org/10.1121/10.0005114
 - Cotter, E., Murphy, P., Bassett, C., Williamson, B., Polagye, B., 2019. Acoustic characterization of sensors used for marine environmental monitoring. Marine Pollution Bulletin 144, 205–215. https://doi.org/10.1016/j.marpolbul.2019.04.079
- Cottier, F., Tverberg, V., Inall, M., Svendsen, H., Nilsen, F., Griffiths, C., 2005. Water mass modification in an Arctic fjord through cross-shelf exchange: The seasonal hydrography of Kongsfjorden, Svalbard. Journal of Geophysical Research:

 Oceans 110. https://doi.org/10.1029/2004JC002757
 - Cowton, T., Slater, D., Sole, A., Goldberg, D., Nienow, P., 2015. Modeling the impact of glacial runoff on fjord circulation and submarine melt rate using a new subgrid-scale parameterization for glacial plumes. Journal of Geophysical Research: Oceans 120, 796–812. https://doi.org/10.1002/2014JC010324
- 955 Cummins, P.F., Armi, L., Vagle, S., 2006. Upstream Internal Hydraulic Jumps. Journal of Physical Oceanography 36, 753–769. https://doi.org/10.1175/JPO2894.1
 - Ćwiąkała, J., Moskalik, M., Forwick, M., Wojtysiak, K., Giżejewski, J., Szczuciński, W., 2018. Submarine geomorphology at the front of the retreating Hansbreen tidewater glacier, Hornsund fjord, southwest Spitsbergen. Journal of Maps 14, 123–134. https://doi.org/10.1080/17445647.2018.1441757
- 960 Demer, D.A., Andersen, L.N., Bassett, C., Berger, L., Chu, D., Condiotty, J., Jr., G.R.C., Hutton, B., Korneliussen, R., Bouffant, N.L., Macaulay, G., Michaels, W.L., Murfin, D., Pobitzer, A., Renfree, J.S., Sessions, T.S., Stierhoff, K.L.,

- Thompson, C.H., 2017. 2016 USA–Norway EK80 Workshop Report: Evaluation of a wideband echosounder for fisheries and marine ecosystem science (report). ICES Cooperative Research Reports (CRR). https://doi.org/10.17895/ices.pub.2318
- Demer, D.A., Berger, L., Bernasconi, M., Bethke, E., Boswell, K., Chu, D., Domokos, R., Dunford, A., Fassler, S., Gauthier, S., Hufnagle, L.T., Jech, J.M., Bouffant, N., Lebourges-Dhaussy, A., Lurton, X., Macaulay, G.J., Perrot, Y., Ryan, T., Parker-Stetter, S., Stienessen, S., Weber, T., Williamson, N., 2015. Calibration of acoustic instruments. (Report). International Council for the Exploration of the Sea (ICES). https://doi.org/10.25607/OBP-185
- Demer, D. A., and Hewitt, R. P. 1993. Calibration of an acoustic echo-integration system in a deep tank, with gain comparisons over standard sphere material, water temperature and time. SC-CAMLR Selected Scientific Papers, 9: 127–144.
 - Ehrenberg, J.E., Torkelson, T.C., 2000. FM slide (chirp) signals: a technique for significantly improving the signal-to-noise performance in hydroacoustic assessment systems. Fisheries Research 47, 193–199. https://doi.org/10.1016/S0165-7836(00)00169-7
- Enderlin, E.M., Hamilton, G.S., 2014. Estimates of iceberg submarine melting from high-resolution digital elevation models:

 application to Sermilik Fjord, East Greenland. Journal of Glaciology 60, 1084–1092.

 https://doi.org/10.3189/2014JoG14J085
 - England, M.R., Eisenman, I., Lutsko, N.J., Wagner, T.J.W., 2021. The Recent Emergence of Arctic Amplification. Geophysical Research Letters 48, e2021GL094086. https://doi.org/10.1029/2021GL094086
- Everett, A., Kohler, J., Sundfjord, A., Kovacs, K.M., Torsvik, T., Pramanik, A., Boehme, L., Lydersen, C., 2018. Subglacial discharge plume behaviour revealed by CTD-instrumented ringed seals. Sci Rep 8, 13467. https://doi.org/10.1038/s41598-018-31875-8
 - Farmer, D., Armi, L., 1999. Stratified flow over topography: the role of small-scale entrainment and mixing in flow establishment. Proc. R. Soc. Lond. A 455, 3221–3258. https://doi.org/10.1098/rspa.1999.0448
 - Farmer, D.M., Dungan Smith, J., 1980. Tidal interaction of stratified flow with a sill in Knight Inlet. Deep Sea Research Part A. Oceanographic Research Papers 27, 239–254. https://doi.org/10.1016/0198-0149(80)90015-1

- Fichefet, T., Poncin, C., Goosse, H., Huybrechts, P., Janssens, I., Le Treut, H., 2003. Implications of changes in freshwater flux from the Greenland ice sheet for the climate of the 21st century. Geophysical Research Letters 30. https://doi.org/10.1029/2003GL017826
- Fonseca, L., Mayer, L., 2007. Remote estimation of surficial seafloor properties through the application Angular Range
 Analysis to multibeam sonar data. Mar Geophys Res 28, 119–126. https://doi.org/10.1007/s11001-007-9019-4
 - Foote, K., Atkins, P., Francis, D., Knutsen, T., 2005. Measuring echo spectra of marine organisms over a wide bandwidth 28.
 - Francois, R. E., and Garrison, G. R. 1982. Sound absorption based on ocean measurements: Part I: Pure water and magnesium sulfate contributions. Journal of the Acoustical Society of America. 72: 896–907.

- Geyer, W.R., Ralston, D.K., 2011. 2.03 The Dynamics of Strongly Stratified Estuaries, in: Wolanski, E., McLusky, D. (Eds.),
 Treatise on Estuarine and Coastal Science. Academic Press, Waltham, pp. 37–51. https://doi.org/10.1016/B978-0-12-374711-2.00206-0
 - Geyer, W.R., Ralston, D.K., Holleman, R.C., 2017. Hydraulics and mixing in a laterally divergent channel of a highly stratified estuary. Journal of Geophysical Research: Oceans 122, 4743–4760. https://doi.org/10.1002/2016JC012455
- Geyman, E.C., J. J. van Pelt, W., Maloof, A.C., Aas, H.F., Kohler, J., 2022. Historical glacier change on Svalbard predicts doubling of mass loss by 2100. Nature 601, 374–379. https://doi.org/10.1038/s41586-021-04314-4
 - Godø, O.R., Handegard, N.O., Browman, H.I., Macaulay, G.J., Kaartvedt, S., Giske, J., Ona, E., Huse, G., Johnsen, E., 2014. Marine ecosystem acoustics (MEA): quantifying processes in the sea at the spatio-temporal scales on which they occur. ICES Journal of Marine Science 71, 2357–2369. https://doi.org/10.1093/icesjms/fsu116
 - Goodman, L., 1990. Acoustic scattering from ocean microstructure. Journal of Geophysical Research: Oceans 95, 11557–11573. https://doi.org/10.1029/JC095iC07p11557

1010

- Goodman, L., and M. J. Forbes, 1990: Acoustic scattering from ocean microstructure. J. Acoust. Soc. Amer., 87 (Suppl.), S6, https://doi.org/10.1121/1.2028334.
- Grabiec, M., Ignatiuk, D., Jania, J. a., Moskalik, M., Głowacki, P., Błaszczyk, M., Budzik, T., Walczowski, W., 2018. Coast formation in an Arctic area due to glacier surge and retreat: The Hornbreen–Hambergbreen case from Spistbergen. Earth Surface Processes and Landforms 43, 387–400. https://doi.org/10.1002/esp.4251
- Hager, A.O., Sutherland, D.A., Amundson, J.M., Jackson, R.H., Kienholz, C., Motyka, R.J., Nash, J.D., 2022. Subglacial Discharge Reflux and Buoyancy Forcing Drive Seasonality in a Silled Glacial Fjord. Journal of Geophysical Research: Oceans 127, e2021JC018355. https://doi.org/10.1029/2021JC018355
- Holbrook, W.S., Páramo, P., Pearse, S., Schmitt, R.W., 2003. Thermohaline Fine Structure in an Oceanographic Front from Seismic Reflection Profiling. Science 301, 821–824. https://doi.org/10.1126/science.1085116
 - Holland, D.M., Thomas, R.H., de Young, B., Ribergaard, M.H., Lyberth, B., 2008. Acceleration of Jakobshavn Isbræ triggered by warm subsurface ocean waters. Nature Geosci 1, 659–664. https://doi.org/10.1038/ngeo316
 - Hopwood, M.J., Carroll, D., Browning, T.J., Meire, L., Mortensen, J., Krisch, S., Achterberg, E.P., 2018. Non-linear response of summertime marine productivity to increased meltwater discharge around Greenland. Nat Commun 9, 3256. https://doi.org/10.1038/s41467-018-05488-8
 - Hopwood, M.J., Carroll, D., Dunse, T., Hodson, A., Holding, J.M., Iriarte, J.L., Ribeiro, S., Achterberg, E.P., Cantoni, C., Carlson, D.F., Chierici, M., Clarke, J.S., Cozzi, S., Fransson, A., Juul-Pedersen, T., Winding, M.H.S., Meire, L., 2020. Review article: How does glacier discharge affect marine biogeochemistry and primary production in the Arctic? The Cryosphere 14, 1347–1383. https://doi.org/10.5194/tc-14-1347-2020
- Howat, I.M., Joughin, I., Scambos, T.A., 2007. Rapid Changes in Ice Discharge from Greenland Outlet Glaciers. Science 315, 1559–1561. https://doi.org/10.1126/science.1138478

- Jackson, R.H., Nash, J.D., Kienholz, C., Sutherland, D.A., Amundson, J.M., Motyka, R.J., Winters, D., Skyllingstad, E., Pettit, E.C., 2020. Meltwater Intrusions Reveal Mechanisms for Rapid Submarine Melt at a Tidewater Glacier. Geophysical Research Letters 47, e2019GL085335. https://doi.org/10.1029/2019GL085335
- Jakacki, J., Przyborska, A., Kosecki, S., Sundfjord, A., Albretsen, J., 2017. Modelling of the Svalbard fjord Hornsund.

 Oceanologia 59, 473–495. https://doi.org/10.1016/j.oceano.2017.04.004
 - Jakobsson, M., Mayer, L.A., Nilsson, J., Stranne, C., Calder, B., O'Regan, M., Farrell, J.W., Cronin, T.M., Brüchert, V., Chawarski, J., Eriksson, B., Fredriksson, J., Gemery, L., Glueder, A., Holmes, F.A., Jerram, K., Kirchner, N., Mix, A., Muchowski, J., Prakash, A., Reilly, B., Thornton, B., Ulfsbo, A., Weidner, E., Åkesson, H., Handl, T., Ståhl, E., Boze,
- L.-G., Reed, S., West, G., Padman, J., 2020. Ryder Glacier in northwest Greenland is shielded from warm Atlantic water by a bathymetric sill. Commun Earth Environ 1, 1–10. https://doi.org/10.1038/s43247-020-00043-0
 - Jech, J.M., 2021. What can you do with twenty years of water column sonar data? Plenty! The Journal of the Acoustical Society of America 149, A61. https://doi.org/10.1121/10.0004515
- Jech, J.M., Michaels, W.L., 2006. A multifrequency method to classify and evaluate fisheries acoustics data. Can. J. Fish.

 Aquat. Sci. 63, 2225–2235. https://doi.org/10.1139/f06-126
 - Jenkins, A., 2011. Convection-Driven Melting near the Grounding Lines of Ice Shelves and Tidewater Glaciers. Journal of Physical Oceanography 41, 2279–2294. https://doi.org/10.1175/JPO-D-11-03.1
 - Jerram, K., Weber, T.C., Beaudoin, J., 2015. Split-beam echo sounder observations of natural methane seep variability in the northern Gulf of Mexico. Geochemistry, Geophysics, Geosystems 16, 736–750. https://doi.org/10.1002/2014GC005429
- Joughin, I., Abdalati, W., Fahnestock, M., 2004. Large fluctuations in speed on Greenland's Jakobshavn Isbræ glacier. Nature 432, 608–610. https://doi.org/10.1038/nature03130
 - Joughin, I., Alley, R.B., Holland, D.M., 2012. Ice-Sheet Response to Oceanic Forcing. Science 338, 1172–1176. https://doi.org/10.1126/science.1226481
 - Kilcher, L.F., Nash, J.D., 2010. Structure and dynamics of the Columbia River tidal plume front. Journal of Geophysical Research: Oceans, 115. https://doi.org/10.1029/2009JC006066

- Kohler, J. Norwegian Polar Institute. (2009). *How close should boats come to the fronts of Svalbard's calving glaciers?*Commissioned report, Governor of Svalbard. Accessed: http://hdl.handle.net/11250/173174
- Konik, M., Darecki, M., Pavlov, A.K., Sagan, S., Kowalczuk, P., 2021. Darkening of the Svalbard Fjords Waters Observed With Satellite Ocean Color Imagery in 1997–2019. Front. Mar. Sci. 8. https://doi.org/10.3389/fmars.2021.699318
- 1055 Kosiba, A., 1960. Some of Results of Glaciological Investigations in SW-Spitsbergen: Carried Out During the Polish I.G.Y. Spitsbergen Expeditions in 1957, 1958 and 1959. Państwowe Wydawn. Nauk.
 - Kowalik, Z., Marchenko, A., Brazhnikov, D., Marchenko, N., 2015. Tidal currents in the western Svalbard Fjords. Oceanologia 57, 318–327. https://doi.org/10.1016/j.oceano.2015.06.003
- Ladroit, Y., Escobar-Flores, and Maurice, A., ESP3: Fisheries acoustics data processing software, SourceForge [EPS3], https://sourceforge.net/p/esp3/wiki/ESP3/, 2023.

- Lavery, A. C., R. W. Schmitt, and T. K. Stanton, 2003: Highfrequency acoustic scattering from turbulent oceanic microstructure: The importance of density fluctuations. J. Acoust. Soc. Amer., 114, 2685, https://doi.org/10.1121/1.1614258.
- Lavery, A.C., Bassett, C., Lawson, G.L., Jech, J.M., 2017. Exploiting signal processing approaches for broadband echosounders. ICES Journal of Marine Science 74, 2262–2275. https://doi.org/10.1093/icesjms/fsx155
 - Lavery, A.C., Chu, D., Moum, J.N., 2010. Measurements of acoustic scattering from zooplankton and oceanic microstructure using a broadband echosounder. ICES Journal of Marine Science 67, 379–394. https://doi.org/10.1093/icesjms/fsp242
 - Lavery, A.C., Geyer, W.R., Scully, M.E., 2013. Broadband acoustic quantification of stratified turbulence. The Journal of the Acoustical Society of America 134, 40–54. https://doi.org/10.1121/1.4807780
- 1070 LeBlanc, L.R., Mayer, L., Rufino, M., Schock, S.G., King, J., 1992. Marine sediment classification using the chirp sonar. The Journal of the Acoustical Society of America 91, 107–115. https://doi.org/10.1121/1.402758
 - Le Boyer, A., Alford, M.H., Couto, N., Goldin, M., Lastuka, S., Goheen, S., Nguyen, S., Lucas, A.J., Hennon, T.D., 2021. Modular, Flexible, Low-cost Microstructure Measurements: The Epsilometer, Journal of Atmospheric and Oceanic Technology 38(3). https://doi.org/10.1175/JTECH-D-20-0116.1
- 1075 Lee, W., Mayorga, E., Setiawan, L., Majeed, I., Nguyen, K., & Staneva, V. (2021). Echopype: A Python library for interoperable and scalable processing of water column sonar data for biological information. arXiv preprint arXiv:2111.00187
 - Leon, G.R., Sandal, G.M., Larsen, E., 2011. Human performance in polar environments. Journal of Environmental Psychology 31, 353–360. https://doi.org/10.1016/j.jenvp.2011.08.001
- Li, J., Roche, B., Bull, J.M., White, P.R., Leighton, T.G., Provenzano, G., Dewar, M., Henstock, T.J., 2020. Broadband Acoustic Inversion for Gas Flux Quantification—Application to a Methane Plume at Scanner Pockmark, Central North Sea. Journal of Geophysical Research: Oceans 125, e2020JC016360. https://doi.org/10.1029/2020JC016360
 - Lilly, D.K., 1978. A Severe Downslope Windstorm and Aircraft Turbulence Event Induced by a Mountain Wave. Journal of the Atmospheric Sciences 35, 59–77. https://doi.org/10.1175/1520-0469(1978)035<0059:ASDWAA>2.0.CO;2
- Loranger, S., Jech, M.J., Lavery, A.C., 2022. Broadband acoustic quantification of mixed biological aggregations at the New England shelf break. The Journal of the Acoustical Society of America 152, 2319–2335. https://doi.org/10.1121/10.0014910
 - Loranger, S., Weber, T.C., 2020. Shipboard Acoustic Observations of Flow Rate From a Seafloor-Sourced Oil Spill. Journal of Geophysical Research: Oceans 125, e2020JC016274. https://doi.org/10.1029/2020JC016274
- 1090 Lurton, X., 2002. An Introduction to Underwater Acoustics: Principles and Applications. Springer Science & Business Media. Lydersen, C., Assmy, P., Falk-Petersen, S., Kohler, J., Kovacs, K.M., Reigstad, M., Steen, H., Strøm, H., Sundfjord, A., Varpe, Ø., Walczowski, W., Weslawski, J.M., Zajaczkowski, M., 2014. The importance of tidewater glaciers for marine mammals and seabirds in Svalbard, Norway. Journal of Marine Systems 129, 452-471. https://doi.org/10.1016/j.jmarsys.2013.09.006

- 1095 MacLennan, D. N. 1981. The theory of solid spheres as sonar calibration targets. Scottish Fisheries Research, 22. 17 pp.
 - Mankoff, K.D., Straneo, F., Cenedese, C., Das, S.B., Richards, C.G., Singh, H., 2016. Structure and dynamics of a subglacial discharge plume in a Greenlandic fjord. Journal of Geophysical Research: Oceans 121, 8670–8688. https://doi.org/10.1002/2016JC011764
- Marston, T.M., Bassett, C., Plotnick, D.S., Kidwell, A.N., Honegger, D.A., 2023. Three-dimensional observations of tidal plume fronts in estuaries using a synthetic aperture sonar array. The Journal of the Acoustical Society of America 154, 1124–1137. https://doi.org/10.1121/10.0020671
 - Martin, L.V., Stanton, T.K., Wiebe, P.H., Lynch, J.F., 1996. Acoustic classification of zooplankton. ICES J Mar Sci 53, 217–224. https://doi.org/10.1006/jmsc.1996.0025
- McGee, T.M., 1990. The Use of Marine Seismic Profiling for Environmental Assessment1. Geophysical Prospecting 38, 861–1105 880. https://doi.org/10.1111/j.1365-2478.1990.tb01879.x
 - McLaren, A.S., Bourke, R.H., Walsh, J.E., Weaver, R.L., 1994. Variability in sea-ice thickness over the North Pole from 1958 to 1992. Geophysical Monograph Series 85, 363–371. https://doi.org/10.1029/GM085p0363
 - Medwin, H., 1977. In situ acoustic measurements of microbubbles at sea. Journal of Geophysical Research (1896-1977) 82, 971–976. https://doi.org/10.1029/JC082i006p00971
- 1110 Medwin, H., Clay, C.S., 1997. Fundamentals of Acoustical Oceanography. Academic Press.

- Mortensen, J., Bendtsen, J., Motyka, R.J., Lennert, K., Truffer, M., Fahnestock, M., Rysgaard, S., 2013. On the seasonal freshwater stratification in the proximity of fast-flowing tidewater outlet glaciers in a sub-Arctic sill fjord. Journal of Geophysical Research: Oceans 118, 1382–1395. https://doi.org/10.1002/jgrc.20134
- Motyka, R.J., Hunter, L., Echelmeyer, K.A., Connor, C., 2003. Submarine melting at the terminus of a temperate tidewater glacier, LeConte Glacier, Alaska, U.S.A. Annals of Glaciology 36, 57–65. https://doi.org/10.3189/172756403781816374
- Moum, J.N., Farmer, D.M., Smyth, W.D., Armi, L., Vagle, S., 2003. Structure and Generation of Turbulence at Interfaces Strained by Internal Solitary Waves Propagating Shoreward over the Continental Shelf. Journal of Physical Oceanography 33, 2093–2112. https://doi.org/10.1175/1520-0485
- Muchowski, J., Umlauf, L., Arneborg, L., Holtermann, P., Weidner, E., Humborg, C., Stranne, C., 2022. Potential and Limitations of a Commercial Broadband Echo Sounder for Remote Observations of Turbulent Mixing. Journal of Atmospheric and Oceanic Technology 39, 1985–2003. https://doi.org/10.1175/JTECH-D-21-0169.1
 - Mugford, R.I., Dowdeswell, J.A., 2011. Modeling glacial meltwater plume dynamics and sedimentation in high-latitude fjords. Journal of Geophysical Research: Earth Surface 116. https://doi.org/10.1029/2010JF001735
- Nam, G. H., Cox, M. G., Harris, P. M., Robinson, S. P., Hayman, G., Beamiss, G. A., Esward, T. J., et al. 2007. A model for characterizing the frequency -dependent variation in sensitivity with temperature of underwater acoustic transducers from historical calibration data. Measurement Science and Technology, 18: 1553 doi:10.1088/0957-0233/18/5/047.
 - Nick, F.M., Vieli, A., Howat, I.M., Joughin, I., 2009. Large-scale changes in Greenland outlet glacier dynamics triggered at the terminus. Nature Geosci 2, 110–114. https://doi.org/10.1038/ngeo394

- Nilsen, F., Cottier, F., Skogseth, R., Mattsson, S., 2008. Fjord-shelf exchanges controlled by ice and brine production: The interannual variation of Atlantic Water in Isfjorden, Svalbard. Continental Shelf Research 28, 1838–1853. https://doi.org/10.1016/j.csr.2008.04.015
 - Oakey, N.S., 1982. Determination of the Rate of Dissipation of Turbulent Energy from Simultaneous Temperature and Velocity Shear Microstructure Measurements.
- Orr, M.H., Haury, L.R., Wiebe, P.H., Briscoe, M.G., 2000. Backscatter of high-frequency (200 kHz) acoustic wavefields from ocean turbulence. The Journal of the Acoustical Society of America 108, 1595–1601. https://doi.org/10.1121/1.1286883
 - Osborn, T.R., 1980. Estimates of the Local Rate of Vertical Diffusion from Dissipation Measurements.

- Palinkas, L.A., Suedfeld, P., 2008. Psychological effects of polar expeditions. The Lancet 371, 153–163. https://doi.org/10.1016/S0140-6736(07)61056-3
- Penrose, J.D., Beer, T., 1981. Acoustic reflection from estuarine pycnoclines. Estuarine, Coastal and Shelf Science 12, 237–249. https://doi.org/10.1016/S0302-3524(81)80122-3
- Promińska, A., Falck, E., Walczowski, W., 2018. Interannual variability in hydrography and water mass distribution in Hornsund, an Arctic fjord in Svalbard. Polar Research.
- Proni, J.R., Apel, J.R., 1975. On the use of high-frequency acoustics for the study of internal waves and microstructure. Journal of Geophysical Research (1896-1977) 80, 1147–1151. https://doi.org/10.1029/JC080i009p01147
- Rignot, E., Koppes, M., Velicogna, I., 2010. Rapid submarine melting of the calving faces of West Greenland glaciers. Nature Geosci 3, 187–191. https://doi.org/10.1038/ngeo765
 - Robertson, C.M., Benn, D.I., Brook, M.S., Fuller, lan C., Holt, K.A., 2012. Subaqueous calving margin morphology at Mueller, Hooker and Tasman glaciers in Aoraki/Mount Cook National Park, New Zealand. Journal of Glaciology 58, 1037–1046. https://doi.org/10.3189/2012JoG12J048
- 1150 Rogers, P. H., and Van Buren, A. L. 1978. New approach to a constant beamwidth transducer. Journal of the Acoustical Society of America, 64: 38–43.
 - Ross, T., Lavery, A., 2009. Laboratory observations of double-diffusive convection using high-frequency broadband acoustics. Exp Fluids 46, 355–364. https://doi.org/10.1007/s00348-008-0570-9
- Ross, T., Lueck, R., 2005. Estimating turbulent dissipation rates from acoustic backscatter. Deep Sea Research Part I:

 Oceanographic Research Papers 52, 2353–2365. https://doi.org/10.1016/j.dsr.2005.07.002
 - Rothrock, D.A., Wensnahan, M., 2007. The Accuracy of Sea Ice Drafts Measured from U.S. Navy Submarines. Journal of Atmospheric and Oceanic Technology 24, 1936–1949. https://doi.org/10.1175/JTECH2097.1
 - Sawada, K., Furusawa, M., Williamson, N.J., 1993. Conditions for the precise measurement of fish target strength in situ. The Journal of the Marine Acoustics Society of Japan 20, 73–79. https://doi.org/10.3135/jmasj.20.73
- Schaffer, J., Kanzow, T., von Appen, W.-J., von Albedyll, L., Arndt, J.E., Roberts, D.H., 2020. Bathymetry constrains ocean heat supply to Greenland's largest glacier tongue. Nat. Geosci. 13, 227–231. https://doi.org/10.1038/s41561-019-0529-x

- Sciascia, R., Straneo, F., Cenedese, C., Heimbach, P., 2013. Seasonal variability of submarine melt rate and circulation in an East Greenland fjord. Journal of Geophysical Research: Oceans 118, 2492–2506. https://doi.org/10.1002/jgrc.20142
- Seim, H.E., Gregg, M.C., Miyamoto, R.T., 1995. Acoustic Backscatter from Turbulent Microstructure. Journal of Atmospheric and Oceanic Technology 12, 367–380. https://doi.org/10.1175/1520-0426(1995)012<0367:ABFTM>2.0.CO;2
 - Serreze, M.C., Francis, J.A., 2006. The Arctic Amplification Debate. Climatic Change 76, 241–264. https://doi.org/10.1007/s10584-005-9017-y
 - Serreze, M.C., Stroeve, J., 2015. Arctic sea ice trends, variability and implications for seasonal ice forecasting. Philosophical Transactions of the Royal Society A: Mathematical, Physical and Engineering Sciences 373, 20140159. https://doi.org/10.1098/rsta.2014.0159
 - Siegert, M., Alley, R.B., Rignot, E., Englander, J., Corell, R., 2020. Twenty-first century sea-level rise could exceed IPCC projections for strong-warming futures. One Earth 3, 691–703. https://doi.org/10.1016/j.oneear.2020.11.002
 - Simmonds, J., MacLennan, D.N., 2008. Fisheries Acoustics: Theory and Practice. John Wiley & Sons.

- Simmons, S.M., Azpiroz-Zabala, M., Cartigny, M.J., b., Clare, M.A., Cooper, C., Parsons, D.R., Pope, E.L., Sumner, E.J.,

 Talling, P.J., 2020. Novel Acoustic Method Provides First Detailed Measurements of Sediment Concentration Structure

 Within Submarine Turbidity Currents. Journal of Geophysical Research: Oceans 125, e2019JC015904.

 https://doi.org/10.1029/2019JC015904
 - Slater, D.A., Carroll, D., Oliver, H., Hopwood, M.J., Straneo, F., Wood, M., Willis, J.K., Morlighem, M., 2022. Characteristic Depths, Fluxes, and Timescales for Greenland's Tidewater Glacier Fjords From Subglacial Discharge-Driven Upwelling During Summer. Geophysical Research Letters 49, e2021GL097081. https://doi.org/10.1029/2021GL097081
 - Slater, D.A., Felikson, D., Straneo, F., Goelzer, H., Little, C.M., Morlighem, M., Fettweis, X., Nowicki, S., 2020. Twenty-first century ocean forcing of the Greenland ice sheet for modelling of sea level contribution. The Cryosphere 14, 985–1008. https://doi.org/10.5194/tc-14-985-2020
- Slater, D.A., Straneo, F., Das, S.B., Richards, C.G., Wagner, T.J.W., Nienow, P.W., 2018. Localized Plumes Drive Front-Wide Ocean Melting of A Greenlandic Tidewater Glacier. Geophysical Research Letters 45, 12,350-12,358. https://doi.org/10.1029/2018GL080763
 - Smyth, W.D., Moum, J.N., 2001. Three-dimensional (3d) Turbulence, in: Steele, J.H. (Ed.), Encyclopedia of Ocean Sciences. Academic Press, Oxford, pp. 2947–2955. https://doi.org/10.1006/rwos.2001.0134
- Stanton, T.K., Chu, D., Jech, J.M., Irish, J.D., 2010. New broadband methods for resonance classification and high-resolution imagery of fish with swimbladders using a modified commercial broadband echosounder. ICES Journal of Marine Science 67, 365–378. https://doi.org/10.1093/icesjms/fsp262
 - Stevens, L.A., Straneo, F., Das, S.B., Plueddemann, A.J., Kukulya, A.L., Morlighem, M., 2016. Linking glacially modified waters to catchment-scale subglacial discharge using autonomous underwater vehicle observations. The Cryosphere 10, 417–432. https://doi.org/10.5194/tc-10-417-2016

- 1195 Straneo, F., Cenedese, C., 2015. The Dynamics of Greenland's Glacial Fjords and Their Role in Climate. Annual Review of Marine Science 7, 89–112. https://doi.org/10.1146/annurev-marine-010213-135133
 - Straneo, F., Curry, R.G., Sutherland, D.A., Hamilton, G.S., Cenedese, C., Våge, K., Stearns, L.A., 2011. Impact of fjord dynamics and glacial runoff on the circulation near Helheim Glacier. Nature Geosci 4, 322–327. https://doi.org/10.1038/ngeo1109
- 1200 Straneo, F., Heimbach, P., 2013. North Atlantic warming and the retreat of Greenland's outlet glaciers. Nature 504, 36–43. https://doi.org/10.1038/nature12854
 - Stranne, C., Mayer, L., Weber, T.C., Ruddick, B.R., Jakobsson, M., Jerram, K., Weidner, E., Nilsson, J., Gårdfeldt, K., 2017. Acoustic Mapping of Thermohaline Staircases in the Arctic Ocean. Sci Rep 7, 15192. https://doi.org/10.1038/s41598-017-15486-3
- Strzelewicz, A., Przyborska, A., Walczowski, W., 2022. Increased presence of Atlantic Water on the shelf south-west of Spitsbergen with implications for the Arctic fjord Hornsund. Progress in Oceanography 200, 102714. https://doi.org/10.1016/j.pocean.2021.102714
 - Sugiyama, S., Minowa, M., Schaefer, M., 2019. Underwater Ice Terrace Observed at the Front of Glaciar Grey, a Freshwater Calving Glacier in Patagonia. Geophysical Research Letters 46, 2602–2609. https://doi.org/10.1029/2018GL081441
- Sutherland, D.A., Jackson, R.H., Kienholz, C., Amundson, J.M., Dryer, W.P., Duncan, D., Eidam, E.F., Motyka, R.J., Nash, J.D., 2019. Direct observations of submarine melt and subsurface geometry at a tidewater glacier. Science 365, 369–374. https://doi.org/10.1126/science.aax3528

- Sutherland, D.A., Straneo, F., 2012. Estimating ocean heat transports and submarine melt rates in Sermilik Fjord, Greenland, using lowered acoustic Doppler current profiler (LADCP) velocity profiles. Annals of Glaciology 53, 50–58. https://doi.org/10.3189/2012AoG60A050
- Swift, C. T., 1980: Passive microwave remote sensing of the ocean—A review. Bound.-Layer Meteor., 18, 25–54, doi:10.1007/BF00117909
- Thorne, P.D., Hanes, D.M., 2002. A review of acoustic measurement of small-scale sediment processes. Continental Shelf Research 22, 603–632. https://doi.org/10.1016/S0278-4343(01)00101-7
- 1220 Thorne, P.D., Hardcastle, P.J., 1997. Acoustic measurements of suspended sediments in turbulent currents and comparison with in-situ samples. The Journal of the Acoustical Society of America 101, 2603–2614. https://doi.org/10.1121/1.418501
 - Thorne, P.D., Hurther, D., 2014. An overview on the use of backscattered sound for measuring suspended particle size and concentration profiles in non-cohesive inorganic sediment transport studies. Continental Shelf Research 73, 97–118. https://doi.org/10.1016/j.csr.2013.10.017
- Thorpe, 1987. Transitional phenomena and the development of turbulence in stratified fluids: A review. Journal of Geophysical Research: Oceans 92, 5231–5248. https://doi.org/10.1029/JC092iC05p05231
 - Turin, G., 1960. An introduction to matched filters. IRE Transactions on Information Theory 6, 311–329. https://doi.org/10.1109/TIT.1960.1057571

- Vagle, S., Chandler, P., Farmer, D.M., 2005. On the dense bubble clouds and near bottom turbulence in the surf zone. Journal of Geophysical Research: Oceans 110. https://doi.org/10.1029/2004JC002603
 - van den Broeke, M.R., Enderlin, E.M., Howat, I.M., Kuipers Munneke, P., Noël, B.P.Y., van de Berg, W.J., van Meijgaard, E., Wouters, B., 2016. On the recent contribution of the Greenland ice sheet to sea level change. The Cryosphere 10, 1933–1946. https://doi.org/10.5194/tc-10-1933-2016
- van Haren, H., Gostiaux, L., 2010. A deep-ocean Kelvin-Helmholtz billow train. Geophysical Research Letters 37. https://doi.org/10.1029/2009GL041890
 - Wagner, T.J.W., Straneo, F., Richards, C.G., Slater, D.A., Stevens, L.A., Das, S.B., Singh, H., 2019. Large spatial variations in the flux balance along the front of a Greenland tidewater glacier. The Cryosphere 13, 911–925. https://doi.org/10.5194/tc-13-911-2019
 - Walczowski, W., 2013. Frontal structures in the West Spitsbergen Current margins. Ocean Science 9, 957–975. https://doi.org/10.5194/os-9-957-2013

- Walczowski, W., Piechura, J., 2006. New evidence of warming propagating toward the Arctic Ocean. Geophysical Research Letters, 33(12). https://doi.org/10.1029/2006GL025872
- Wawrzyniak, T., Osuch, M., 2020. A 40-year High Arctic climatological dataset of the Polish Polar Station Hornsund (SW Spitsbergen, Svalbard). Earth System Science Data 12, 805–815. https://doi.org/10.5194/essd-12-805-2020
- Weber, T.C., Ward, L.G., 2015. Observations of backscatter from sand and gravel seafloors between 170 and 250 kHz. The Journal of the Acoustical Society of America 138, 2169–2180. https://doi.org/10.1121/1.4930185
 - Weidner, E., Stranne, C., Sundberg, J.H., Weber, T.C., Mayer, L., Jakobsson, M., 2020. Tracking the spatiotemporal variability of the oxic–anoxic interface in the Baltic Sea with broadband acoustics. ICES Journal of Marine Science 77, 2814–2824. https://doi.org/10.1093/icesjms/fsaa153
- Weidner, E., Weber, T.C., 2024. Broadband acoustic characterization of backscattering from a rough stratification interface.

 The Journal of the Acoustical Society of America 155, 114–127. https://doi.org/10.1121/10.0024148
 - Weidner, E. 2025. Angular dependence of backscattering between 170 and 250 kHz from the terminus of a tidewater glacier. The Journal of the Acoustical Society of America 158(1): 504-514, https://doi.org/10.1121/10.0037196.
- Weidner, E., Weber, Thomas.C., Mayer, L., Jakobsson, M., Chernykh, D., Semiletov, I., 2019. A wideband acoustic method for direct assessment of bubble-mediated methane flux. Continental Shelf Research 173, 104–115. https://doi.org/10.1016/j.csr.2018.12.005
 - Xu, G., Bemis, K., Jackson, D., Ivakin, A., 2021. Acoustic and In-Situ Observations of Deep Seafloor Hydrothermal Discharge:
 An OOI Cabled Array ASHES Vent Field Case Study. Earth and Space Science 8, e2020EA001269.
 https://doi.org/10.1029/2020EA001269
- 1260 Xu, G., Jackson, D.R., Bemis, K.G., 2017. The relative effect of particles and turbulence on acoustic scattering from deep sea hydrothermal vent plumes revisited. The Journal of the Acoustical Society of America 141, 1446–1458. https://doi.org/10.1121/1.4974828

- Xu, Y., Rignot, E., Fenty, I., Menemenlis, D., Flexas, M.M., 2013. Subaqueous melting of Store Glacier, west Greenland from three-dimensional, high-resolution numerical modeling and ocean observations. Geophysical Research Letters 40, 4648–4653. https://doi.org/10.1002/grl.50825
 - Xu, Y., Rignot, E., Menemenlis, D., Koppes, M., 2012. Numerical experiments on subaqueous melting of Greenland tidewater glaciers in response to ocean warming and enhanced subglacial discharge. Ann. Glaciol. 53, 229–234. https://doi.org/10.3189/2012AoG60A139
- Young, R.A., Merrill, J.T., Clarke, T.L., Proni, J.R., 1982. Acoustic profiling of suspended sediments in the marine bottom boundary layer. Geophysical Research Letters 9, 175–178. https://doi.org/10.1029/GL009i003p00175